Doctoral Dissertation

Enhancement of Thermoelectric Properties of Sb-based Bulk Materials by Crystal Structure Design

(結晶構造制御によるアンチモン含有バルク材料の熱電特性の向上)

GUANGHE LI

July 2014

Graduate School of Engineering,
Osaka University

Thesis Advisors:

Professor Shinsuke Yamanaka, Ph.D.

Associate Professor Ken Kurosaki, Ph.D.

Yamanaka Laboratory, Division of Sustainable Energy and Environmental Engineering, Graduate School of Engineering, OSAKA UNIVERSITY

Thesis Committee:

Professor Shinsuke Yamanaka, Ph.D.

Professor Takao Yamamoto, Ph.D.

Associate Professor Ken Kurosaki, Ph.D.

Associate Professor Hiroshi Nishikawa, Ph.D.

Graduate School of Engineering

OSAKA UNIVERSITY

CONTENTS

Table of Contents
List of Figures
List of Tables

CHAPTER PAGES

I. INTRODUCTION

II. Experimental Methods

List of Figures

List of Tables

CHAPTER I

Introduction

1.1 Background of Thermoelectric Materials

The fossil fuel brought unprecedented glory to human society. Unfortunately, the average efficiencies of power generation are very limited, only about 40% of the energy we can use, while the remaining 60% are wasted as thermal energy and so on.[1)] In addition, excessive exploitation of natural resources makes it nearly depleted. Moreover, the burning production CO_2 results in the global warming. And such global climate changing is becoming increasing alarming. In one words, we are facing the depletion of nature resources and a serious environmental problems, ex.), air pollution and the global warming and so on. However, about 90 % of world's energy consumption is still dependent on the fossil fuel even today.2)

Therefore, search for new friendly environmental energy sources recently became of major importance in our modern societies. One way to improve the efficiency of power generation is through the recycling of waste heat with thermoelectric generators as shown in Figure 1.1[3)] Consequently, the electricity generation from waste heat via thermoelectric materials can be seen as a new "green" energy source. The conversion of waste heat into electrical energy may play an important role in present challenge to develop alternative energy technologies to reduce our dependence on fossil fuels and reduce the greenhouse gas emissions. In addition, they can also be used in solid-state refrigeration devices (base on Peltier effect, details shown in next section).

Radioisotope thermoelectric generators (RTGs) are used as power supply in the space application by NASA. Power-generation applications are currently being investigated by the automotive industry as a means to develop electrical power from waste engine heat from the radiator and exhaust systems for use in next-generation

vehicles. In addition, TE refrigeration include seat coolers (heater) for comfort and electronic component cooling (a small scale cooling applied in computer) and so on.[4)]

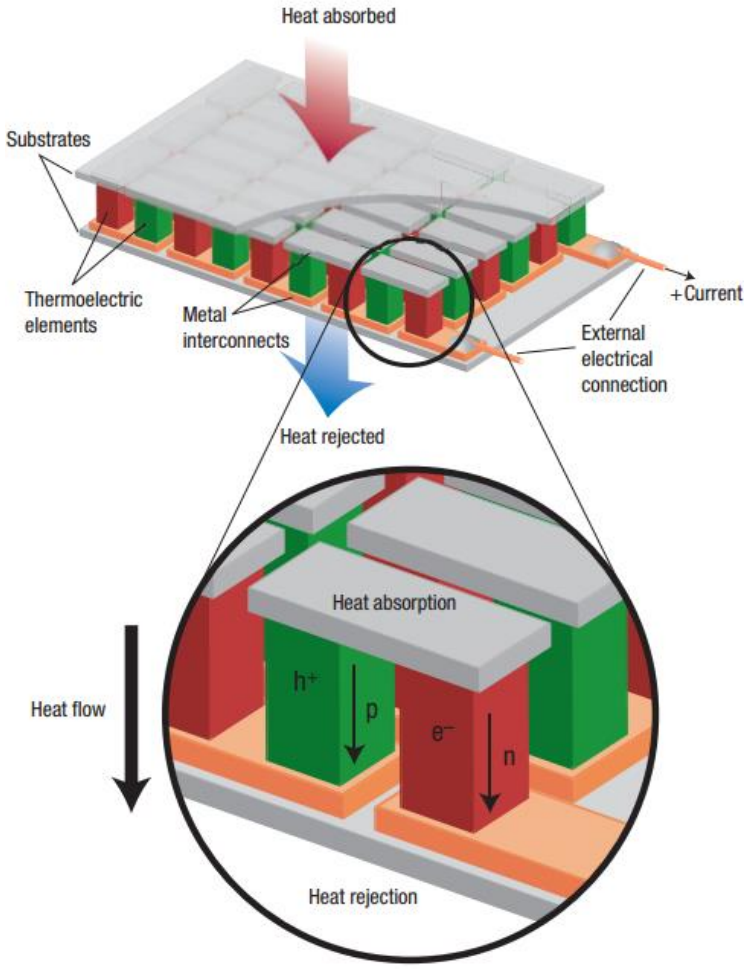

Figure 1.1 Thermoelectric module showing the direction of charge flow on both cooling and power generation.[3)]

For those reasons, recent two decades, thermoelectric material (TE) has attracted much attention due to the direct energy conversion from waste heat to electrical power, and could be an important part of the solution to future power supply and sustainable energy management.

1.2 Thermoelectric Phenomena

1.2.1 Seebeck Effect

The development of TE materials was started from Thomas Johann Seebeck's accidental 1820s discovery that a compass needle deflected when placed in the vicinity of a closed loop formed from two dissimilar metal conductors if the junctions were maintained at different temperatures.[5-8] In the beginning, Seebeck believed that it was induced by magnetism. However, it was quickly realized that it was an electrical current induced from temperature difference between two junctions of materials as shown in Figure 2. In other words, the temperature difference produces an electric potential (Voltage) which can drive an electric current in a closed circuit. This is the so called Seebeck effect. And the magnitude of the voltage was proportional to the temperature difference and depended on the type of conducting material as shown in equation 1.1:

$$V = S\left(T_H - T_C\right) \tag{1.1}$$

where, V is the potential voltage, T_H and T_C are the hot and cold temperatures forming the temperature gradient, and the proportionality constant (S) is known as the Seebeck coefficient or thermopower. And, the Seebeck voltage (V) does not depend on the distribution of temperature along the metals between the junctions. Such voltage or current production across the junctions of two different materials is caused due to the diffusion of electrons from high electron density region to low electron density region as the density of electrons is different in different materials. If the temperature are same on the both junctions, equal amount of electron will diffuses from each sides and drive toward to the opposite directions, thus the net current is zero, and if both the junctions are kept at different temperature then diffusion at both the junctions are different amount of current is produced. Therefore, the net current is not zero. This is known as the phenomena of thermoelectricity.

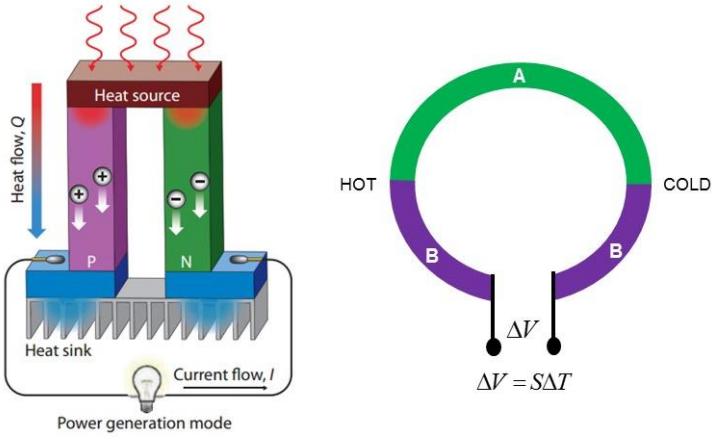

Figure 1.2 Schematic illustrations of a thermoelectric module for power generation and Seebeck effect.[9)]

1.2.2 Peltier Effect

The converse phenomena versus to the Seebeck effect is the so called Peltier effect, which was discovered by Jean Charles Athanase Peltier in 1834. And it states that a temperature difference created by applying a voltage between two electrodes connected to a sample of semiconductor material. In other words, an electrical current would produce heating or cooling at the junction of two dissimilar metals as shown in Figure 3.[10)] The Peltier coefficient (Π) is described as following equation;

$$\Pi = \frac{1}{I}\frac{dQ_{AB}}{dt} \tag{1.2}$$

where, dQ_{AB}/dt and I are the rate of heat transfer at the junction and the electrical current, respectively. This phenomenon can be useful when it is necessary to transfer heat from one medium to another on a small scale. For example, Peltier-effect devices are used for thermoelectric cooling in electronic equipment and computers when more conventional cooling methods are impractical.

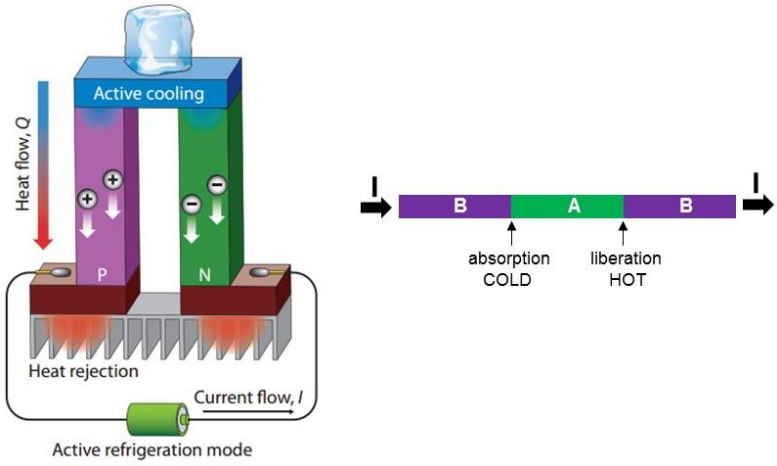

Figure 1.3 Schematic illustrations of a thermoelectric module for active refrigeration and Peltier effect.[9)]

1.2.3 Thompson Effect

Thompson effect is the last one of three types of thermoelectric effect. And it describes that the radiation or absorption of heat energy from a material that has both temperature and voltage gradients. The Thompson effect states that in the absence of Joule heating, the heat gained or lost is given by

$$\tau = \frac{dQ_T}{IdtdT} \tag{1.3}$$

where, τ, Q_T, I and T are the Thomson coefficient, heat, electrical current, spatial coordinate and temperature, respectively. It should be noted that the Seebeck and Peltier coefficients describe heat transfer in a system consist of two dissimilar materials, while the Thompson effect describes heat flow in a single material. From the Tompson effect, it can be shown that

$$\tau_1 - \tau_2 = \frac{dS_{12}}{dT} \tag{1.4}$$

and consequently that[11)]

$$\Pi_{12} = S_{12}T \tag{1.5}$$

The equation 1.5 shows that the Thomson effect leads to a direct relationship between the Seebeck and Peltier coefficient.

1.2.4 Thermoelectric Efficiency

Like all heat engines, thermoelectric generators are bound by the Carnot limit on efficiency.

$$\eta_{Carnot} = \frac{\Delta T}{T_H} = \frac{T_H - T_C}{T_H} \tag{1.6}$$

Thermoelectric device performance relies directly on the temperature gradient (ΔT) and thermoelectric figure of merit (ZT).[3)]

$$\eta = \eta_{Carnot}\eta_D = \frac{T_H - T_C}{T_H} \cdot \frac{\sqrt{1+ZT_M} - 1}{\sqrt{1+ZT_M} + \frac{T_C}{T_H}} \tag{1.7}$$

where, T_H and T_C are the temperature of the hot and cold ends in a thermoelectric module and T_M is the average temperature. And ZT is the so called dimensionless figure of merit.

This equation imply that the energy conversion efficiency of thermoelectric device will never exceed the Carnot efficiency. Figure 1.4 shows that for a ZT = 1 and a temperature gradient of 400K, the efficiency is around 10%. To increase the efficiency, it is necessary to increase ZT or to increase the temperature gradient. In other words, the TE materials should have high ZT, and stable at high temperature.

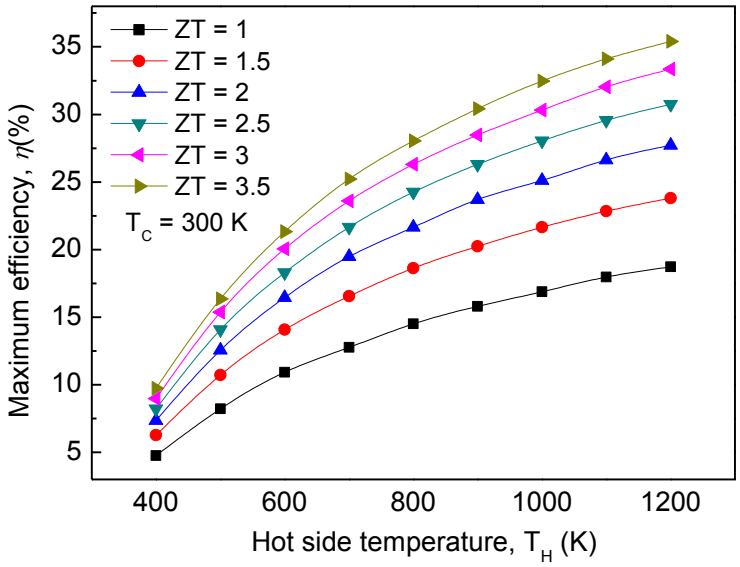

Figure 1.4 Temperature dependence of thermoelectric energy conversion efficiency with various values of *ZT*.

1.2.5 Optimization of Thermoelectric Figure of Merit

The primary index for evaluation of thermoelectric materials is the dimensionless figure of merit, *ZT*

$$ZT = \frac{S^2\sigma}{\kappa}T = \frac{S^2\sigma}{\kappa_{ele} + \kappa_{lat}}T \tag{1.8}$$

This equation indicates that the dimensionless figure of merit, *ZT* is proportional to the Seebeck coefficient (*S*), and electrical conductivity (σ), but inversely proportional to the thermal conductivity (κ). Therefore, an enhancement of *ZT* need to improve electrical properties (*S*, σ), meanwhile, reduce the thermal conductivity (κ). However, the electronic contribution to the thermal conductivity (κ_{ele}) has strongly interrelated to the electrical conductivity ($\kappa_{ele} = L\sigma T$), thus the independent control is difficult. In addition, *S* and σ is also interrelated closely through carrier concentration (*n*). Unfortunately, the higher *n* the higher σ, and the lower *S*.

$$S = \frac{8\pi^2 k_B^2 T}{3qh^2} m^* \left(\frac{\pi}{3n} \right)^{2/3} \tag{1.9}$$

where, m^* is the effective mass of the carrier. Therefore, the optimization process for carrier concentration should be carry out for maximizing the power factor ($S^2\sigma$) as shown in Figure 1.5. This figure indicates that the maximum $S^2\sigma$ and ZT located in the carrier concentration of 10^{19} ~ 10^{21} carriers per cm^3, which fall in between common metals and semiconductors, that is, the concentration must be found in heavily doped semiconductors.

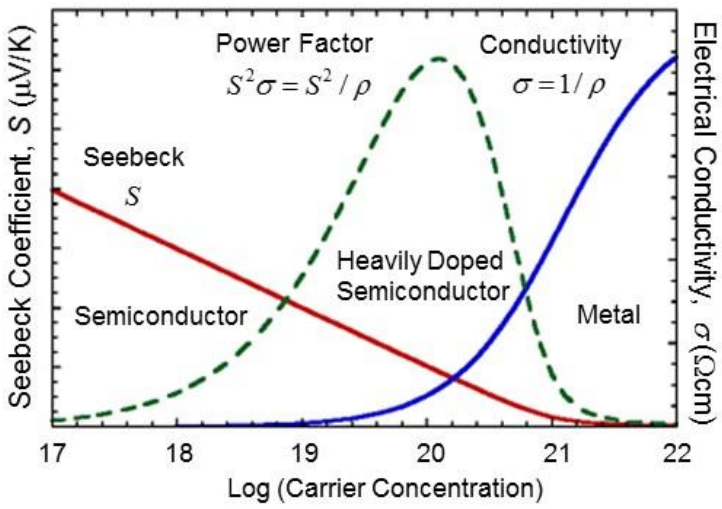

Figure 1.5 Carrier concentration dependence of electrical conductivity σ, Seebeck coefficient S, and power factor $S^2\sigma$.[12)]

1.2.5.1 Electrical Conductivity

At the simple level, electrical conductivity can be describe as the product of the carrier concentration (*n*), the charge per carrier (*e*), and the charge mobility (μ).

$$\sigma = ne\mu \tag{1.10}$$

Correspondingly, the electrical resistivity is the reciprocal of electrical conductivity, and describe how strongly a given material opposes the flow of electric current.

$$\rho = \frac{1}{\sigma} \tag{1.11}$$

The Wiedemann-Franz law describes a general relationship between electronic contribution of the thermal conductivity (κ_{ele}) to the electrical conductivity (σ) of a metal, and the ratio is proportional to the temperature (*T*).[13)]

$$\frac{\kappa_{ele}}{\sigma} = LT \tag{1.12}$$

where, *L* known as the Lorenz number, is equal to

$$L = \frac{\kappa}{\sigma T} = \frac{\pi^2}{3}\left(\frac{\kappa_B}{e}\right)^2 = 2.44\times10^{-8} W\Omega K^{-2} \tag{1.13}$$

The functions shown in above, indicating that a fixed ration between thermal conductivity and electrical conductivity, meaning that a large Seebeck coefficient is required to produce a high energy conversion efficiency in thermoelectric devices. For metals or degenerate semiconductors, the Seebeck coefficient (*S*) is given by:[14)]

$$S = \frac{8\pi^2 k_B^2}{3eh^2} m^* T\left(\frac{\pi}{3n}\right)^{2/3} \tag{1.9}$$

Equation (1.9) shows that low carrier concentration insulators and even semiconductors have large Seebeck coefficient. However, low carrier concentration also results in low electrical conductivity according to the equation (1.10).

1.2.5.2 Carrier Concentration

In the case of semiconductor, there is a band-gap energy E_g between valence band and empty band which is appreciably greater than that of kT. The concentration of electrons in the intrinsic semiconductor is equal to the concentration of holes and is given by

$$n_e = n_h = 2\left(\frac{2\pi kT}{h^2}\right)^{3/2}\left(m_e^* m_h^*\right)^{3/4}\exp\left(-\frac{E_g}{2kT}\right) \tag{1.14}$$

where, h is Planck's constant, m_e^* and m_h^* are the effective masses of the electron and hole respectively. And they depend on the strength of interactions between the electron and holes and the lattice. And the sigh might be positive or negative, and the values might be larger or smaller than the rest mass of electrons. And since,

$$\sigma = |e|\left(n_e\mu_e + n_h\mu_h\right) \tag{1.15}$$

The electrical conductivity in semiconductor can be written as,

$$\sigma = \left[2|e|\left(\frac{2\pi kT}{h^2}\right)^{3/2}\left(m_e^* m_h^*\right)^{3/4}\exp\left(-\frac{E_g}{2kT}\right)\right]\left(\mu_e + \mu_h\right) \tag{1.16}$$

where, E_g is the band gap energy at room temperature for materials. From the equation mentioned above, the inherent conductivity and carrier concentration strongly dominated by the ratio between band gap and temperature, $E_g/ k_B T$. And the larger $E_g/2k_B T$ the lower carrier concentration, result in a lower electrical conductivity.

1.2.5.3 Carrier Mobility

The carrier mobility is defined as the magnitude of velocity of charge carrier in a unit strength of electric filed.

$$\mu = |v| / E \tag{1.17}$$

In electric filed, the sigh of velocity of electrons and holes is opposite. The velocity of charge carrier in electric filed known as,

$$v = q\tau E / m \tag{1.18}$$

where, τ is the relaxation time, *E* is the electric filed strength, and *m* is the mass of particle. Thus, the velocities of electrons and holes can be written as,

$$\mu_e = e\tau_e / m_e, \quad \mu_h = e\tau_h / m_h \tag{1.19}$$

The carrier's mobility affected by several types of scattering effect. Lattice scattering, which result from thermal vibrations of the lattice and increases with the increasing amplitude of vibrations at higher temperature. Impurity scattering, which distort the periodicity of the lattice. And grain boundary scattering and so on. However, mobility is not strongly dependent on temperature, thus, the electrical conductivity has a temperature dependence which is mostly determined by the carrier concentration.

1.2.5.4 Effective Mass

The effective mass of the charge carrier provides another conflict as large effective masses produce high thermopower (*S*) but low electrical conductivity. The m^* in equation (1-9) refers to the density-of-states effective mass, which increases with flat, narrow bands with high density of states at the Fermi surface. However, as the inertial effective mass is also related to m^*, heavy carriers will move with slower velocities, and therefore small mobility, which in turn leads to low electrical conductivity (equation 1-10). The exact relationship between effective mass and mobility is complex, and depends on electronic structure, scattering mechanisms and isotropy.[12)]

A balance must be found for the effective mass (or bandwidth) for the dominant charge carrier, forming a compromise between high effective mass and high mobility. High mobility and low effective mass is typically found in materials made from elements with small electronegativity difference, whereas high effective masses and low mobilities are found in materials with narrow bands such as ionic compounds. It is not obvious which effective mass is optimum; good thermoelectric materials can be found within a wide range of effective masses and mobilities: from low-mobility, high-effective-mass polaron conductors (oxides,[15)] chalcogenides[16)]) to high-mobility, low-effective-mass semiconductors (SiGe, GaAs).

From Figure 1.6, we also get an information why thermoelectric research is concentrated in semiconductors instead of metals or insulators. In the beginning, metals were used to forming the basis of thermocouple operation, however, their extremely large thermal conductivity make them as poor thermoelectric generators. And, in the case of insulators, the insufficient current flows are the fatal demerit for using as high efficient thermoelectric materials. Let us return to the subject that maximizing the *ZT* we have talked above. Except optimizing the carrier concentration, reduce the thermal conductivity is another way to approach a high *ZT*. Although, electrical thermal conductivity hard to be depressed without lower the electrical properties. However, the lattice thermal conductivity, which induced from lattice

vibration, can be operate without affect the electrical properties, results in a remarkable enhancement in *ZT*.

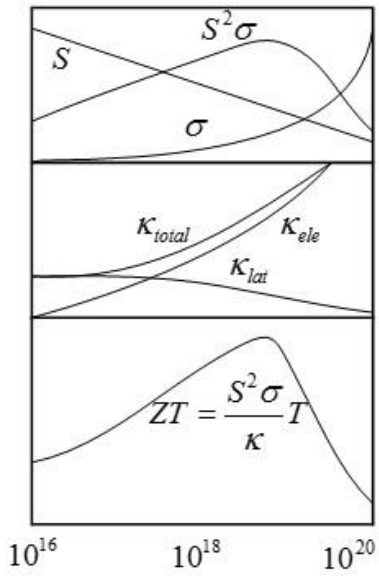

Figure 1.6 Carrier concentration dependence of thermoelectric properties.

1.2.5.5 Thermal Conductivity

Intuitively, thermal conductivity includes mainly two components: an electronic contribution (κ_{ele}), due to the movement of carriers, and a lattice contribution via the phonons (κ_{lat}), due to the vibration of lattice.

$$\kappa = \kappa_{ele} + \kappa_{lat} \tag{1.20}$$

According to the Wiedemann-Franz law, the electronic part of the thermal conductivity is related to the electronic conductivity.

$$\kappa_{ele} = L\sigma T \tag{1.21}$$

where, L is the Lorenz number. In metals, it is equal to,

$$L = \frac{\pi^2}{3}\left(\frac{k_B}{e}\right)^2 = 2.44\times10^{-8} W\Omega K^{-2} \quad (1.13)$$

and the lattice contribution to the thermal conductivity can be expressed as,

$$\kappa_{\text{lat}} = \frac{1}{3} C_V v l \quad (1.22)$$

where, C_V is molar heat capacity, v is sound velocity, and l is phonon mean free path. And C_V can be expressed as,

$$C_V = 9Nk_B\left(\frac{T}{\theta}\right)^3 \int_0^{x_D} \frac{x^4 e^x}{(e^x-1)^2} dx, \quad x_D = \theta/T \quad (1.23)$$

Where, N is number of atoms, k_B is Boltzmann constant, and θ is the Debye temperature. And, the simple estimation of the minimum lattice thermal conductivity, $\kappa_{\text{lat.min}}$ can be estimated by using the lattice constant instead of phonon mean free path.

$$\kappa_{\text{lat}\cdot\text{min}} = \frac{1}{3} C_V v l_{\text{lat}} \quad (1.24)$$

In this case, l_{lat} is the lattice constant.

Alloying is a proven approach to reduce the lattice thermal conductivity as shown in Figure 1.7.[17] The figure shows that alloying have a little effect on power factor, but have a much lower thermal conductivity than the constituent members. Therefore, alloying have a positive impact on ZT due to the strongly reduced thermal conductivity. This is precisely why almost thermoelectric materials are alloys.

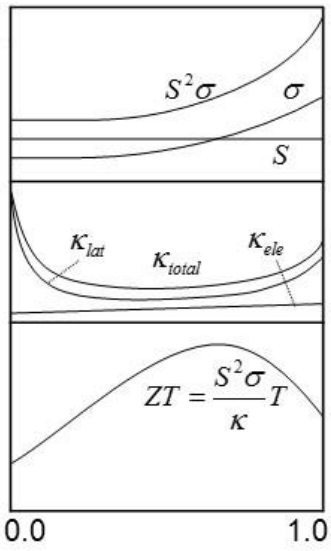

Figure 1.7 Impact of alloying on the components of *ZT* as a function of alloy composition for an arbitrary thermoelectric alloy.

Current thermoelectric technology is based on several classical TE materials, for example, Bi_2Te_3/Sb_2Te_3, PbTe, TAGS, Si-Ge and so on. However, due to the high toxicity of Pb and Te, and the concerns about the rising cost of Te, Bi_2Te_3 and PbTe based TE materials are facing serious limitation in real applications. Ge is rare metal, thus too expensive for module fabrication. In comparison, cobalt and antimony are inexpensive, and influence minimal hazard to people or environment among skutterudites family. And, due to the ideal mechanical properties for module fabrication, as well as the high TE performance in the intermediate temperature range, $CoSb_3$ based skutterudites were considered as the most potential TE materials in automobile application.

1.3 Skutterudite Thermoelectrics

The name of Skutterudites was derived from a naturally occurring mineral, skutterudite or $CoAs_3$, first found in Skutterud, Norway. It possess a cubic crystal structure with 32 atoms per unit cell. A schematic showing the basic structure of the

Skutterudite unit cell is shown in Figure 1.8, and a more detailed description of the crystal structure is given in the next section.

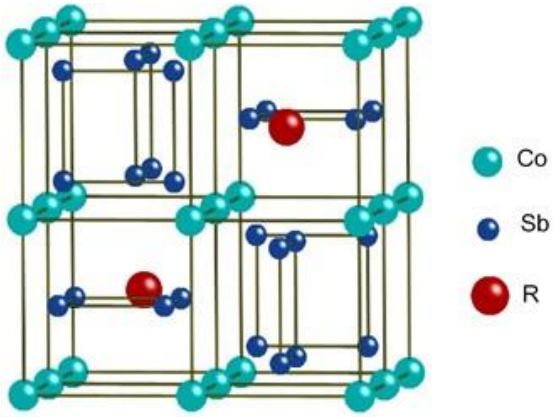

Figure 1.8 Crystal structure of Skutterudites.

As described by Slack, the binary Skutterudite compounds possesses the basic conditions for high *ZT* values, i.e. a large unit cell, heavy constituent atom masses, low electronegativity differences between the constituent atoms, and large carrier mobilities. In addition, Skutterudites form covalent structures with low coordination numbers for the constituent atoms and thus can incorporate atoms in the relatively large voids formed. Therefore, compounds can be formed with atoms filling the voids of the Skutterudites structure.[12)]

Although, the binary Skutterudites have shown such interesting electronic properties, however, due to the high thermal conductivities, the thermoelectric performance was poor. The best TE material should possess thermal properties similar to that of a glass and electrical properties similar to that of a perfect single crystal materials, i.e. PGEC concept was first introduced by Slack.[12)] In other words, a poor thermal conductor and a good electrical conductor are needed simultaneously. As first predicted by Slack, placing atoms in the interstitial voids of this crystal system would substantially reduce thermal conductivity by introducing phonon-scattering centers. Hence, these atomic void-fillers would rattle about in their oversized cages,

thereby providing an approach to drastically reduce thermal conductivity and maximize *ZT*.[12] Nowadays, the filled-skutterudites were widely studied and have proven that have potential to meet such PGEC criteria, i.e. through filling process, the lattice thermal conductivity was reduced remarkably while maintaining the appealing power factor characteristics of the binary Skutterudites system.[18-20] The special open cage-like crystal structure make the filling process possible. The details about the crystal structure are described as below.

1.3.1 Crystal Structure Features of Skutterudites

The general formula of Skutterudites compounds is composition of MX_3 (*M* = Co, Rh, Ir; *X* = P, As, Sb). The Skutterudites structure have a body centered cubic structure with the space group *Im*3. The crystallographic unit cell consists of eight MX_3 units, with the eight M atoms occupying the *c* sites (1/4, 1/4, 1/4), and the 24 *X* atoms occupying the *g* sites (0, *y*, *z*). And the unit cell M_8X_{24} includes two large voids with positions of (0, 0, 0) or (1/2, 1/2, 1/2) as illustrated in Figure 1.9. Such a cage-like structure is the most special characteristic of the skutterudites. The remaining six octants of the structure contain four planar X_4 rings, which are mutually orthogonal and run parallel to the cubic crystallographic axes, while a cubic framework of transition metal cations bounds the cell.

In the skutterudite structure, each *X* atom has four nearest neighbors, two *X*-*X* bonds and tow *M*-*X* bonds, form a distorted tetrahedron at corners as shown in Figure 1.9. Both bond distances of the *M*-*X* and *X*-*X* are short and nearly equal to the sum of the covalent radius, indicating that a strong covalent bonding exist between *M*-*X* atoms and *X*-*X* atoms. In contrast, the bond distance of *M*-*M* is relatively large, indicating that a weak bonding occurs between *M*-*M* atoms.

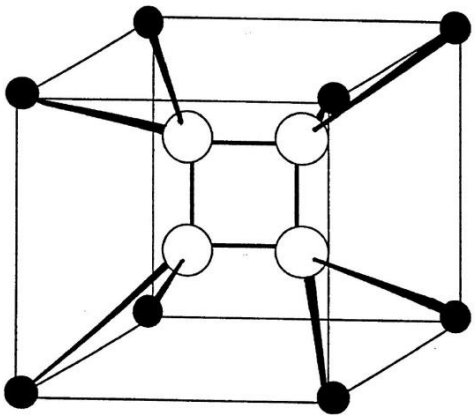

Figure 1.9 Coordination of *X* atoms (white spheres) in the skutterudite structure. Pnicogen atom (*X*) s form a planar rectangular cluster. Each pnicogen atom has four near neighbors: two pnicogen atoms and two *M* atoms (Black spheres).[20)]

1.3.2 Filled Skutterudites

As mentioned before, the most interesting point in the skutterudite structure is that there are two large lattice voids, and each of the voids is surrounded by 12 *X* atoms in the structure as shown in Figure 1.10. Therefore, instead of the general formula of binary skutterudites, MX_3, the chemical formula can be expressed as $\square M_4X_{12}$, where $\square$ represents the presence of the void.

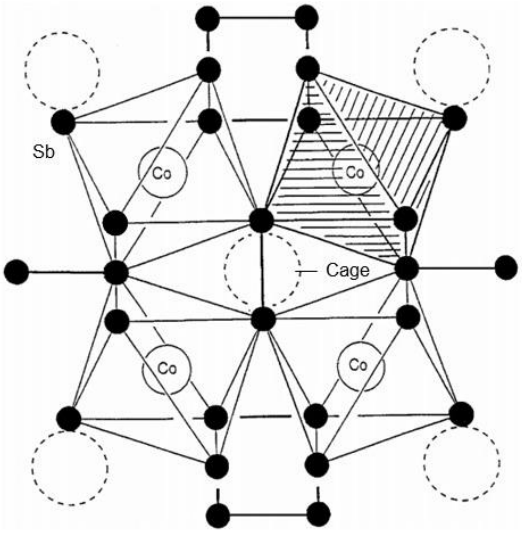

Figure 1.10 The skutterudite unit cell.[21)]

This is a quite large void in the structure as shown in Table 1. Therefore, it is capable of accommodation by many different foreign atoms with different ionic sizes. By filling guest atoms into the skutterudites voids, filler elements donate their valence electrons to the conduction bands of the materials, so that filling of the cages with various atoms can lead to an optimum electron concentration to maximize the power factor. In the meantime, the filler atoms are bound weakly with the host atoms and rattle, result in acting as phonon scattering center to reduce lattice thermal conductivity effectively. Therefore, filled skutterudites were assumed to be potential candidates as ideal PGEC materials.

As mentioned before, among the skutterudites, $CoSb_3$ is the most studied for the practical application due to its reasonable band gap of ~ 0.2 eV, high carrier mobility,[22] and the fact that it is composed of inexpensive and environmentally benign constituent elements as compared to other skutterudite compounds. It has been widely studied that the cages in $CoSb_3$ can be fully or partially filled with a variety of different atoms, including alkali metals (Li, Na, and K),[23-25] alkaline earth elements (Ca, Sr, and Ba),[26-28] rare-earth elements (La, Ce, Yb, Eu, Nd, and Sm),[29-34] and other elements (Ga, In, and Tl).[35-39] The electron concentration in partially filled skutterudites ($R_yCo_4Sb_{12}$) is determined by the filling fraction (y) and the effective charge state of the filler atoms in a system with perfect chemical stoichiometric ratio.

Table 1.1 The void radius of binary skutterudites compounds[21]

Compound	Void Radius (Å)	Compound	Void Radius (Å)
CoP_3	1.763	$RhSb_3$	2.024
$CoAs_3$	1.825	IrP_3	1.906
$CoSb_3$	1.892	$IrAs_3$	1.931
RhP_3	1.909	$IrSb_3$	2.040
$RhAs_3$	1.934		

For a particular guest atom in filled $CoSb_3$, FFLs (filling fraction limits) is the only factor to adjust electrical and thermal transport properties.[40] Due to there are no electron-deficient elements in partial filled skutterudites, constricted by the valence balance law, the filling amounts of fillers are limited. According to the previous works, the FFLs and the effective charge states for various foreign atoms are summarized as shown in Table 1.2.

Although, the various different species were partially filled into the cages, however, the effect on electrical transport properties are almost same at a given electron concentration. The effective masses of the carrier electrons and the thermopowers on a given carrier concentrations shows almost identical value even with various different fillers. The primary reason is that in partially filled skutterudites, fillers donate their outermost valence electrons into the framework but do not significantly affect the electronic structure near the bottom of the conduction bands.[40] In other words, the characteristics of the electron density of states (DOS), especially in the position close to the bottom of the conduction band, are very similar to each other for *n*-type partially filled skutterudites, which also leads to a similar trend in electrical transport properties for those *n*-type materials. In a word, electron concentration determines the electrical properties for *n*-type partially filled skutterudites, regardless filler spices.

And the carrier concentration for approaching the maximum power factors was considered around 0.4-0.6 electrons per Co_4Sb_{12}.[40] However, the lattice thermal conductivity obtain much different effect from different filler atoms. For phonon resonant scattering, only the lattice phonons with the frequencies close to the rattling modes of fillers could be scattered. And consider the localized vibration frequencies of filler atoms are different each other, double or multiple filling might scatter the lattice phonon spectra as broad as possible, result in an enhancement of *ZT*. The Figure 1.11 shows the literature results for single-, double-, and multiple-filled Skutterudites. Compare to the single-filling, the double- and multiple-filling show more effective to enhance the *ZT*.

Table 1.2 The summary of experimental filling fraction limits, carrier concentration and the maximum *ZT* for different filler atoms in Co_4Sb_{12}.

Ele.	FFLs	n_H ($10^{20}cm^{-3}$)	ZT_{max}	Ele.	FFLs	n_H ($10^{20}cm^{-3}$)	ZT_{max}
Li (+1)		2	1.3	Eu (+2)	60%	10.1	0.9
Na (+1)		3.8	1.2	Nd (+3)	10%	0.41	0.45
K (+1)	45%		1	Sm (+3)			0.8
Ca (+2)			0.45	Ga (+1)	2%	0.15	0.18
Sr (+2)	40%	3.8	0.9	In (+1)	8%		0.7
Ba (+2)	44%		1.1	Tl (+1)	22%	2.39	0.9
La (+3)	23%	1.7		Sn		0.38	0.2
Ce (+3)	10%	2.4					
Yb (+2)	25%	2.3	1.2				

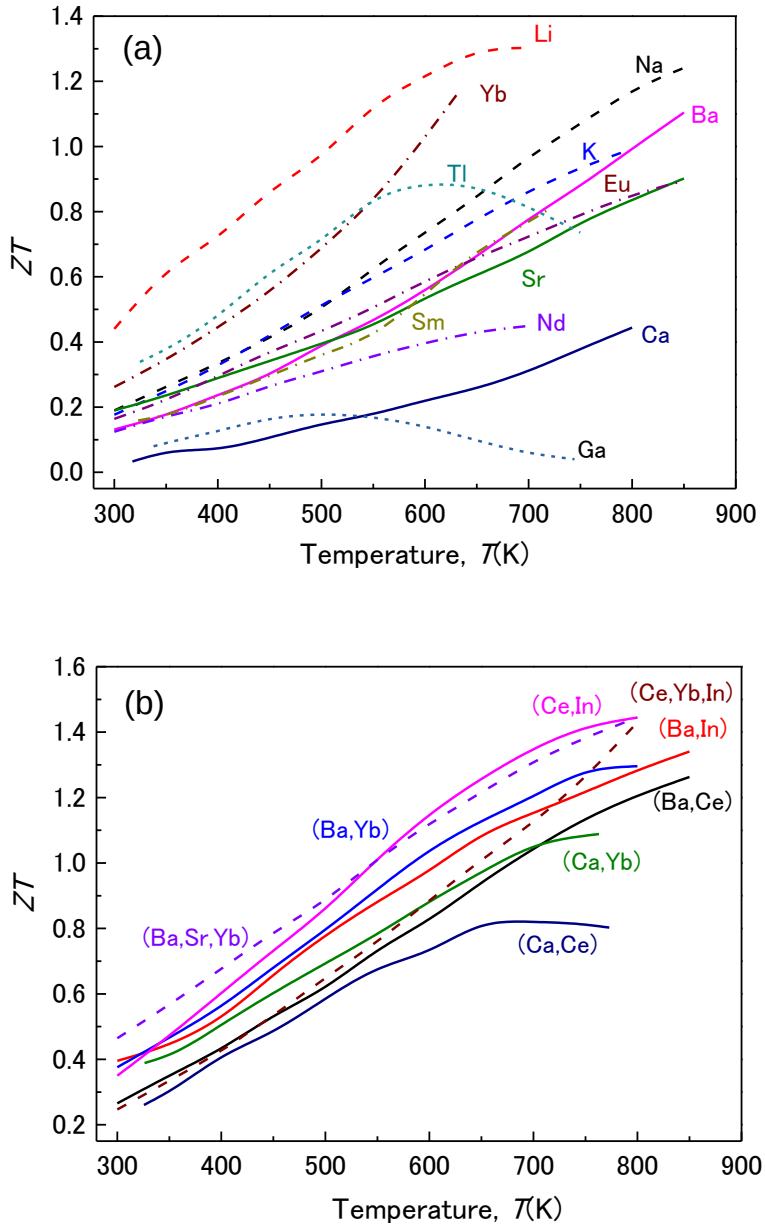

Figure 1.11 Temperature dependence of *ZT* for reported (a) single-filled and (b) double- and multiple-filled Skutterudites.

1.3.3 Mechanical Properties of Skutterudites

Except the high *ZT* value, ideal mechanical properties is also important for module fabrication. Compare to other high performance TE materials within intermediate temperature range (PbTe, Zn_4Sb_3), $CoSb_3$ based Skutterudites shows more large potential in real application as shown in Table 3.

Table 1.3 Comparison of the mechanical properties between $CoSb_3$, PbTe and Zn_4Sb_3.

Compounds	Melting Point (K)	Thermal expansion ($10^{-6}K^{-1}$)	Young's Modulus (GPa)	Poison ratio	Fracture strength (MPa)
$CoSb_3$ [41]	1149	9-10	135-140	0.20	111
N-PbTe [42]	1197	20	50	0.22	70
Zn_4Sb_3 [43]	841	-	57.9-76.3	-	56.6-83.4

Compare with PbTe which shows high performance, it has a comparable melting point and approximately half of thermal expansion coefficient, and an about 3-times elastic constant. In addition, the destruction strength is high compared with PbTe, and the thermal shock tolerance computed from these values is very as high as $CoSb_3$: 246 to PbTe: 140. The thermal expansion coefficient of Skutterudite is even close to aluminum Al_2O_3 (~$7x10^{-6}$ K^{-1}) which is a typical insulation material, and since *N* and *P*-type are made with a material of the same kind, when forming an element, it is not necessary to take into consideration the thermal expansion difference between *N* and *P*-type materials. And, although the Zn_4Sb_3 also shows very high *ZT*, however due to the relative low melting point and brittleness, it can't be used for module manufacturing.

1.4 Half-Heusler Thermoelectrics

Half-Heusler (HH) compounds is one of potential thermoelectric materials for high-temperature application. HH compounds crystallize in the space group of zinc blende (*F*43*m*), consisting of three interpenetrating fcc sublattices and one vacant sublattice. HH have chemical formula of *XYZ*, where, *X* and *Y* are transition metals and *Z* is a main-group element. The least and most electronegative elements *X* are at (1/2, 1/2, 1/2) and *Z* at (0, 0, 0) forming a rock salt lattice. *Y* are found at (1/4, 1/4, 1/4) in the centers of tetrahedral formed by *Z*, as well as by *X* as shown in Figure 1.12.[44-46)] The Heusler intermetallic compounds with fully filled sublattices are metals (full-Heuler alloys), whereas the vacant *Y* atom sites in half-Heusler compounds give rise to narrow bands result in semiconducting characteristics.[47)]

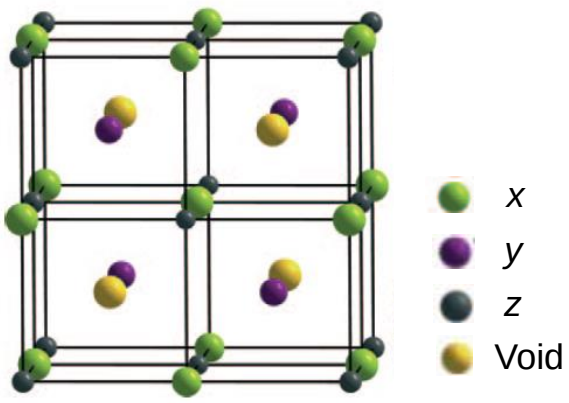

Figure 1.12 Crystal structure of Half-Heusler compound.

The most attractive feature of HH compounds as promising thermoelectric materials is the large room-temperature Seebeck coefficients of ~100 μVK^{-1} and moderate electrical resistivities of ~1-10 $\mu\Omega m$. In addition, their high melting point of 1100-1300 °C as well as their chemical stability with essentially zero sublimation at temperature near 1000 °C is other advantages for HH alloys.47)

There are several ways to improve TE properties in the class of HH alloys. Doping on the *Z* site provides the charge carriers, to approach the optimization of

carrier concentration. And doping on the *X* and *Y* sites can conduces mass fluctuation disorder that result in the reduction of thermal conductivity. And the typical several HH compounds which with significantly enhanced *ZT* is shown as Figure 1.13.[48-50)]

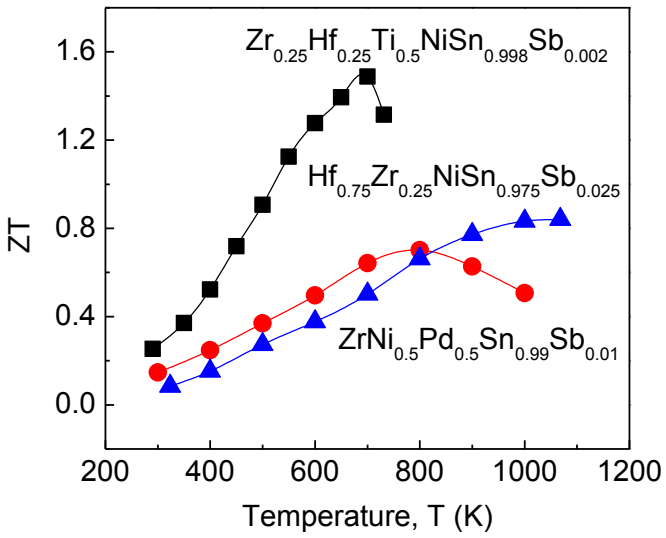

Figure 1.13 Temperature dependence of *ZT* for reported Half-Heusler compounds.[48-50)]

As introduced above, a most important factor in developing TE energy conversion technologies is the development of higher-performance TE materials, either completely new materials or existing materials. In the present thesis, the TE properties of the classic Sb-based bulk TE materials were studied, i.e.) $CoSb_3$ based Skutterudies compounds with group 13 elements filling and half-heusler compound with noble elements (Pt). Both of them show high TE-performance in the intermediate and high temperature range and ideal mechanical properties, thus researches for enhancement of TE performance of such potential bulk TE materials have significant meaning for future application.

Our group has studied two of group 13 elements Ga-[38] and Tl-[39] single filled $CoSb_3$ based skutterudites; Both of Ga and Tl are effective for phonon scattering, especially Tl single-filled one showed the maximum *ZT* of 0.9. However, there is no

report about In single-filled $CoSb_3$ based skutterudites. Therefore, I have selected the In single-filled skutterudites as my first research topic and the results were described in chapter III.

In addition, compare with the Tl single-filled one, In-Tl double-filled skutterudites showed more effective phonon scattering effect, [51] resulted in lower lattice thermal conductivity and higher *ZT*. From the previous results, I expected that the group 13 elements triple-filling would scatter phonons more effectively. Therefore, I have studied the TE properties of group 13 elements triple-filled skutterudites as my second research object and the results were described in chapter IV.

In order to achieve the further reduction of lattice thermal conductivity, I selected Tl which is a heaviest element in group 13 elements and K which is one of the lightest elements double-filled skutterudites as the third research object to expect scattering a broader range of heat carrying phonons and the results were described in chapter V.

And in chapter VI, the TE properties of noble element contained half-heusler compound PtYSb was studied.

Finally, the summary and conclusions of this thesis were given in chapter VII.

References

1) W.H.J. Graus, M. Voogt, and E. Worrell, Energy Policy **35**, 3936 (2007).
2) http://www.heat2power.net/en_scope.php.
3) G.J. Snyder and E.S. Toberer, Nature materials **7**, 105 (2008).
4) T. M. Tritt and M.A. Subramanian, MRS Bulletin **31**, 188 (2006).
5) Seebeck, T.J., Ueber den magnetismus der galvenische kette, Abh. K. Akad. Wiss. Berlin, 289, 1821.
6) Seebeck, T.J., Magnetische polarization der metalle und erze durck temperature-differenz, Abh. K. Akad. Wiss. Berlin, 265, 1823.
7) Seebeck, T.J., Ann. Phys. (Leipzig) [2] **6**, 1(1826).
8) Seebeck, T.J., Methode, Platinatiegel auf ihr chemische reinheit durck thermomagnetismus zuprufen, Schweigger's J. Phys. **46**, 101(1826).
9) J. Li, W. Liu, L. Zhao and M. Zhou, NPG Asia Mater. **2**, 152 (2010).
10) Peltier, J.C.A., Nouvelles experiences sur la caloricite des courants electrique, Ann. Chem. Phys. 56, 371(1834).
11) G.S. Nolas, J. Sharp, and H.J. Goldsmid. Thermoelectrics: Basic Principles and New Materials Developments (Springer, Berlin, 2001).
12) D.M. Rowe, CRC Handbook of Thermoelectrics (CRC Press, New York, 1995)
13) Jones, Theoretical Solid State Physics
14) R.W. Fritts, Thermoelectric Materials and Devices (Reinhold, New York, 1960).
15) K. Koumoto, I. Terasaki, and R. Funahashi, Mat. Res. Soc. Bull. 31, 206 (2006).
16) G.J. Snyder, T. Caillat, and J.P. Fleurial, Phys. Rev. B. 62, 10185(2000).
17) A.F. Ioffe, *Semiconductor Thermoelements and Thermoelectric Cooling*, Infosearch, London(1957).
18) D.T. Morelli and G.P. Meisner, J. Appl. Phys. **77**, 3777(1995).
19) X.Y. Zhao, X. Shi, L.D. Chen, W.Q. Zhang, W.B. Zhang, and Y.Z. Pei, J. Appl. Phys. **99**, 053711(2006).
20) Z. Zhou, C. Uher, A. Jewell, and T. Caillat, Phys. Rev. B **71**, 235209(2005).
21) G.S. Nolas, D.T. Morelli, and T.M. Tritt, Annu. Rev. Mater. Sci. **29**, 89(1999).

22) C. Uher, in Recent Trends in Thermoelectric Materials Research I, Semiconductors and Semicmetals, edited by T. M. Tritt, Academic Press, San Diego, Vol. **69**, 139(2001).
23) J.J. Zhang, B. Xu, L.M. Wang, D.L. Yu, Z.Y. Liu, J. L. Heand Y.J. Tian:Appl. Phys. Lett. **98**, 072109(2011).
24) Y.Z. Pei, J. Yang, L.D. Chen, W. Zhang, J. R. Salvadorand J.H. Yang:Appl. Phys. Lett. **95**, 042101(2009).
25) Y.Z. Pei, L.D. Chen, W. Zhang, X. Shi, S.Q. Bai, X. Y. Zhao, Z. G. Meiand X.Y. Li:Appl. Phys. Lett. **89**, 221107(2006).
26) M. Puyet, B. Lenoir, A. Dauscher, M. Dehmas, C. Stieweand E. Muller:J. Appl. Phys. **95**, 4852(2004).
27) X.Y. Zhao, X. Shi, L.D. Chen, W.Q. Zhang, W. B. Zhangand Y.Z. Pei:J. Appl. Phys. **99**, 053711(2006).
28) L.D. Chen, T. Kawahara, X.F. Tang, T. Goto, T. Hirai, J.S. Dyck, W. Chen and C. Uher:J. Appl. Phys. **90**, 1864(2001).
29) G.S. Nolas, J.L. Cohn and G.A. Slack:Phys. Rev. B **58**,164(1998).
30) D.T. Morelli, G. P. Meisner, B. X. Chen, S. Q. Huand C. Uher:Phys. Rev. B **56**, 7376(1997).
31) J. Yang, Q. Hao, H. Wang, Y. C. Lan, Q. Y. He, A. Minnich, D. Z. Wang, J. A. Harriman, V. M. Varki, M. S. Dresselhaus, G. Chen and Z. F. Ren: Phys. Rev. B 80, 115329(2009).
32) G. A. Lamberton, Jr., S. Bhattacharya, R. T. Littleton IV, M. A. Kaeser, R. H. Tedstrom and T. M. Tritt: Appl. Phys. Lett. **80**, 598(2002).
33) V. L. Kuznetsov, L. A. Kuznetsova and D. M. Rowe: J. Phys.: Condesns. Matter **15**, 5035(2003).
34) Y. P. Jiang, X. P. Jia, T. C. Su, N. Dong, F. R. Yu, Y. J. Tian, W. Guo, H. W. Xu, L. Deng and H. A. Ma: J. Alloy. Compd. **493**, 535(2009).
35) T. He, J. Chen, D. Rosenfeld and M. A. Subramanian: Chem. Mater. **18**, 759 (2006).
36) R. C. Mallik, C. Stiewe, G. Karpinski, R. Hassdorf and E. Muller: J. Electron. Mater. **38**, 1337(2009).

37) B. C. Sales, B. C. Chakoumakos and D. Mandrus: Phys. Rev. B **61**, 2475(2000).
38) A. Harnwunggmoung, K. Kurosaki, T. Plirdpring, T. Sugahara, Y. Ohishi, H. Muta and S. Yamanaka: J. Appl. Phys. **110**, 013521(2011).
39) A. Harnwunggmoung, K. Kurosaki, H. Muta and S. Yamanaka: Appl. Phys. Lett. **96**, 202107(2010).
40) X. Shi, S. Bai, L. Xi, J. Yang, W. Zhang, and L.D. Chen, J. Mater. Res. **26**, 1745 (2011).
41) R.D. Schmidt, E.D. Case, J.E. Ni, J.S. Sakamoto, R.M. Trejo, E. Lara-Curzio, Philosophical Magazine, **92**, 727 (2012).
42) J.R. Salvador, J. Yang, X. Shi, H. Wang, A.A. Wereszczak, H. Kong, C. Uher, Philosophical Magazine, **89**, 1517 (2009).
43) J.R. Sootsman, D.Y. Chung, and M.G. Kanatzidis, Angew. Chem. Int. Ed. 48, 8616 (2009).
44) W. Jeischko, Metall. Trans. A 1, 3159(1970).
45) S. J. Poon, in Recent Trends in Thermoelectric Materials Research II, edited by T.M. Tritt, Semiconductors and Semimetals, 70, 37(Academic Press, New York, 2001).
46) H.C. Kandpal, C. Felser, and R. Seshadri, J. Phys. D: Appl. Phys. 39, 776 (2006).
47) J. R. Sootsman, D. Y. Chung, and M. G. Kanatzidis, Angew. Chem. Int. Ed. 48, 8616(2009).
48) S. Sakurada and N. Shutoh, Appl. Phys. Lett. 86, 082105(2005).
49) Q. Shen, L. Chen, T. Goto, T. Hirai, J. Yang, G.P. Meisner, and C. Uher, Appl. Phys. Lett. 79, 25(2001).
50) G.S. Nolas, J. Poon, and M. Kanaatzidis, MRS Bulletin 31, 199(2006).
51) A. Harnwunggmoung, K. Kurosaki, A. Kosuga, M. Ishimaru, T. Plirdpring, R. Yimnirun, J. Jutimoosik, S. Rujirawat, Y. Ohishi, H. Muta, and S. Yamanaka, J. Appl. Phys. 112, 043509 (2012).

CHAPTER II

Experimental Methods

2.1 Characterization Analysis

2.1.1 X-ray Diffraction Analysis

The sample can be identified by using the *X*-ray diffraction (XRD) analysis technique. Figure 2-1 illustrates the basic principle of XRD according to Bragg's law.[1)] Consider a set of lattice planes (*hkl*), of equidistance *d* (*hkl*). Consider an incident plane wave of wave vector $\boldsymbol{k_0}$ and of incidence angle θ with respect to the planes. The incident angle θ, called the Bragg angle, is the complementary angle to the conventional incident angle in optics. Any points of one lattice plane (*hkl*) are scattering waves being in phase in a direction $\boldsymbol{k}$ which corresponds to the classical reflection law. If this condition is met, the optical path difference between the waves scattered by two adjacent planes is therefore the same whatever the position of the points in the planes, in particular between two points *O* and O' on a normal common to the planes; it follows easily from Figure 2.1 that:

$$\delta = HO + OK = 2d\sin\theta \tag{2.1}$$

The in-phase condition, called the *Bragg condition* (or Bragg law or Bragg equation), becomes accordingly

$$2d\sin\theta = n\lambda \tag{2.2}$$

where, λ is the wavelength and *n* is an integer called diffraction (or reflection) order. A set of *d-spaces* obtained from a single compound will represent the set of planes that can pass through the atoms and can be used for comparison with sets of *d-spaces* obtained from standard compounds.

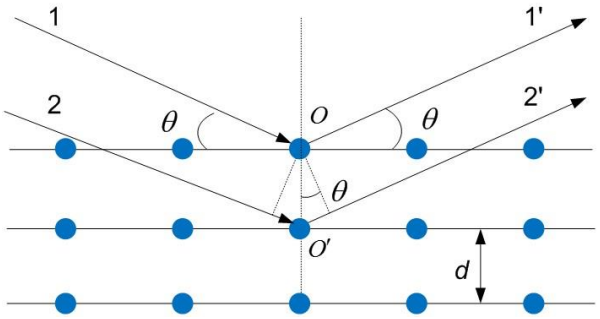

Figure 2.1 The relationship between wavelength, atomic spacing (*d*) and angle (θ) is described by the Bragg equation.

In the most common layout of the resulting powder diffractrometer, the ray diagram is derived from the focusing camera, as explained by Figure 2.2. The diffractrometer is operated through a continuous (θ, 2θ) rotation. The amplified and integrated detector output is fed into a chart recorder with calibrated and adjustable paper speed. In recent diffractometers, the recorder is often replaced by a video display screen which enables computer processing of the diffraction pattern.

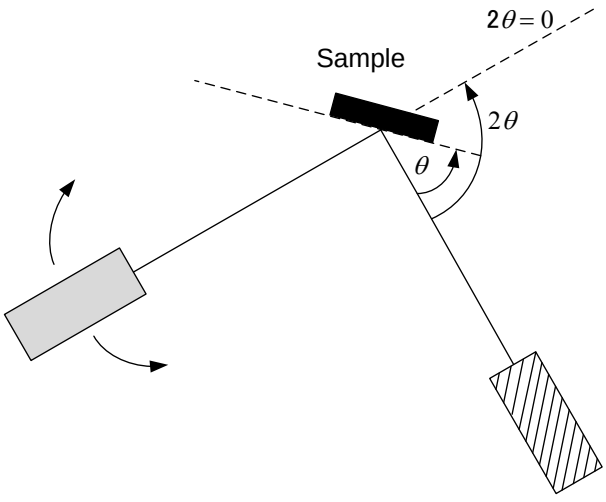

Figure 2.2 Schematic illustration of X-ray diffracting apparatus.

In this research, X-ray diffraction (XRD) measurements were performed on a Rigaku, RINT2000/PC series. The lattice parameters, unit cell volume and theoretical density were estimated from the XRD results. When X-ray radiation passes through the matter, the radiation interacts with the electrons in the atoms, resulting in scattering of the radiation. If the atoms are regularly organized in planes (i.e. the matter is crystalline) and the distances between the atoms are of the same magnitude as the wavelength of the X-rays, constructive and destructive interference of the scattered X-rays will occur. These result in diffraction in which X-rays are emitted at characteristic angles based on the spaces between the atomic planes in the crystal structure. Most crystals have many sets of planes passing through their atoms. Each set of planes has a specific interlunar distance and will give rise to a characteristic angle for diffracted X-rays.

2.1.2 Morphology of Surface Microstructure

The surface microstructure measurements were revealed by the Scanning electron microscopy (SEM). The SEM was assessed as early as 1935 by knoll,[1)] i.e. at about the same time and by the same research group as the conventional TEM. Whereas the later soon developed, the SEM had to wait until the 1960s for practicing the implementation. Its development has been closely kinked to the progress of electronics and video techniques. The SEM was used to observe microstructures of the samples. In this thesis, the SEM observations were performed on a Hitachi High Technologies, S-2600H. The schematic diagram of the SEM equipment is shown as outlined in Figure 2.3.

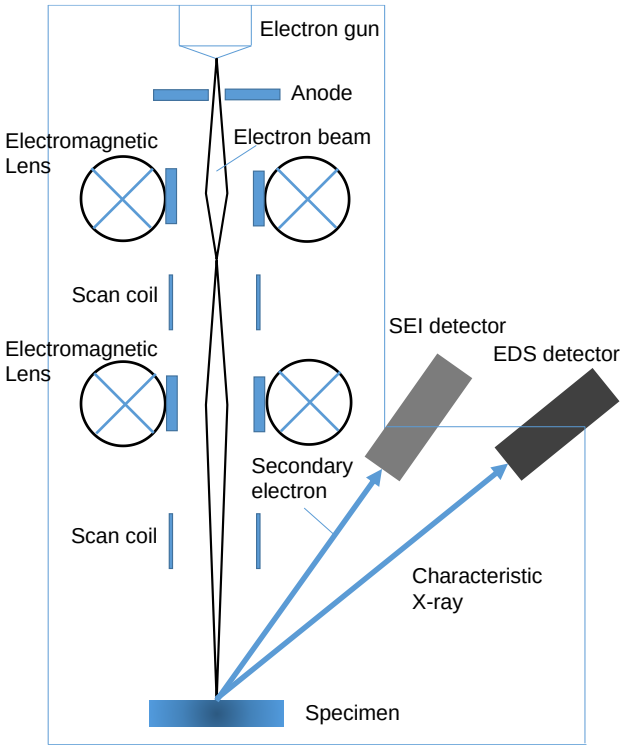

Figure 2.3 Schematic illustration of SEM.[2)]

2.2 Electrical Resistivity and Seebeck Coefficient

The electrical resistivity measurement was performed in a helium atmosphere using the thermopower measuring device (ULVAC ZEM-1). The schematic view of equipment is shown in Figure 2.4.

The electrical resistivity was measured by the standard four probe method with a constant current of approximately 100 mA. The electrical resistivity is represented by the following equation:

$$\rho_{sample} = \frac{V_{sample}}{V_{ref}} R_{ref} \frac{A_{sample}}{L_{sample}} \tag{2.3}$$

where, V_{sample} is the measured voltage between two probes placed on the sample, R_{ref} is a standard resistor incorporated into the equipment, V_{ref} is the voltage dropped across the standard resistor, A_{sample} is the cross section of the sample, and L_{sample} is

the distance between two thermocouples on the sample. The Seebeck coefficients were also measured using ULVAC ZEM-1 in helium atmosphere and over the temperature range of 300-973 K. The Seebeck coefficient (*S*) is given by the following equation:

$$S = \frac{V_{sample}}{T_H - T_L} \tag{2.4}$$

where, T_H and T_L are the measured absolute temperatures at the two points from which V_{sample} was measured. The measurement was carried out by applying three temperature gradients of ΔT: 20, 30, and 40 K between two blocks at each temperature *T*, the average value of three data is used as the experimental value.

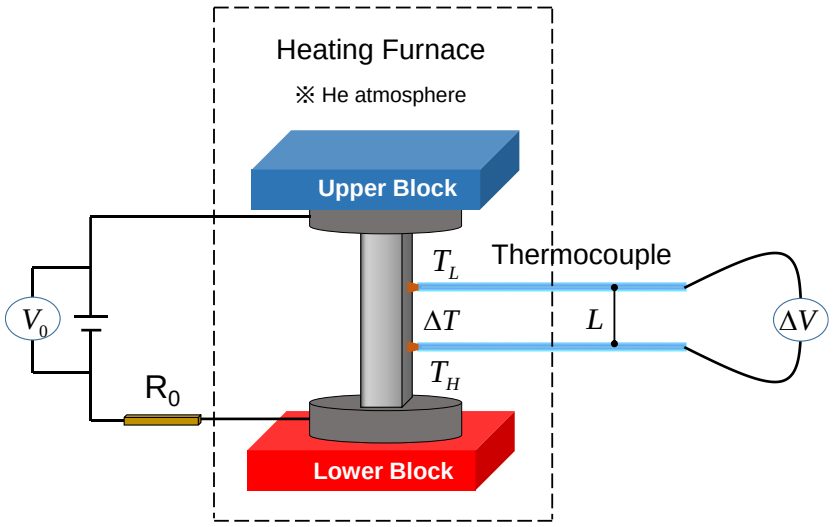

Figure 2.4 Schematic illustrating of the electrical resistivity and the Seebeck coefficient measurement.

2.3 Thermal Conductivity

The thermal properties of the bulk samples can be measured by the laser flash thermal diffusivity (LFTD) method. The laser flash method is by far the most favored for measuring the thermal diffusivity (α) of bulk samples at temperatures well above ambient. A typical apparatus is shown in Figure 2.5. The sample, typically a wafer, whose diameter is much greater than the thickness (*L*), is irradiated on one face with pulses of laser light not more than a millisecond long. The temperature of the opposite face of the sample is monitored, perhaps with an infrared sensor.

In this thesis, the systems of measurement on thermal diffusivity (α) by laser flash method (Thermal-constantan Analyzer, ULVAC, TC 7000) in vacuum (Figure 2.5). In the complete absence of heat loss from the sample, the temperature would rise monotonically to a limiting value. In a real situation, the measured temperature will peak and then return to ambient temperature. The time required to reach one-half of the peak temperature at the rear face of the specimen, $t_{1/2}$ can be used to determine *α* according to

$$\alpha = \frac{1.37L^2}{\pi^2 t_{1/2}} \tag{2.5}$$

The thermal conductivity (κ) is calculated from the temperature rise vs. time profile. The thermal diffusivity is related to the thermal conductivity as shown below:

$$\kappa = \alpha d C_p \tag{2.6}$$

where, κ is the thermal conductivity of the specimens, *d* is the experimental density , and C_p is the heat capacity.

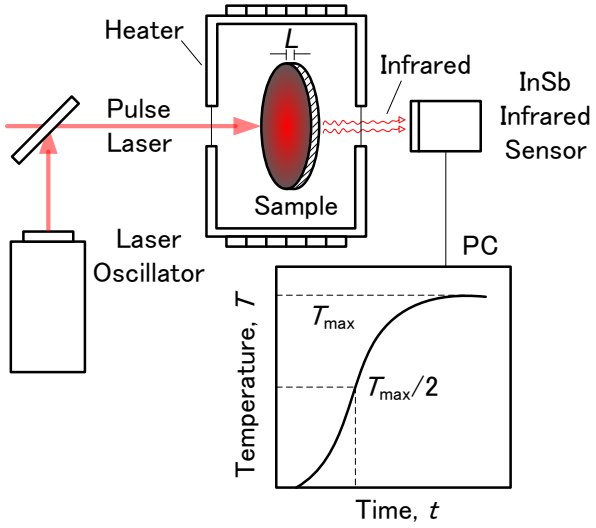

Figure 2.5 Schematic illustrating of the thermal diffusivity measurement.

The densities (*d*) of the samples were calculated from the measured weight and dimensions. Density is a measure of mass per unit of volume. The higher an object's density, the higher it's mass per volume. A denser object (such as iron) will have less volume than an equal mass of some less dense substance (such as water). The unit of density is the kilogram per cubic meter (kg/m^3).

The heat capacity (C_p) approaches the classical value *3nR* at high temperature, i.e. above the Debye temperature, while at low temperature C_p varies according to the T^3 law of Debye.[3)] In the present research, $C_p = 3nR$ is used for estimated the heat capacity of the samples.

2.4 Sound velocity

The elastic moduli are consisting of the shear modulus (G), Young's modulus (E), Bulk modulus (k), Bulk compressibility (β), and Debye temperature (θ_D). These parameters are evaluated from sound velocities of the samples. The sound velocities, i.e. longitudinal velocity (V_L) and shear velocity (V_S), of the sample were measured by an Ultrasonic pulse echo method (Nihon Matech, Echometer 1062). The schematic view of the apparatus is shown in Figure 2.6.

The sound velocities in the sample can be calculated from the sample length and the time separation between the ultrasonic echoes.[4] The longitudinal sound velocity (V_L) and shear sound velocity (V_S) are described by the following equation:

$$V_L = \frac{2L}{T_2 - T_1} \tag{2.7}$$

$$V_S = \left[\left(\frac{T_3 - T_2}{D} \right)^{1/2} + \left(\frac{T_2 - T_1}{2L} \right)^{1/2} \right]^{-1/2} \tag{2.8}$$

In equation (2.7) and (2.8), T_1 is the reflection time of the longitudinal sound velocity from the bottom face of the sample, T_2 is the reflection time of the longitudinal sound velocity from the top face of the sample, T_3 is the reflection time of the shear sound velocity from the top face of the sample, D is the diameter of the sample, and L is the length of the sample. A 5.0 MHz longitudinal wave pulse and shear wave pulse were used for measuring the longitudinal sound velocity (V_L) and the shear sound velocity (V_S), respectively.

In case of isotropic materials, the Debye temperature (θ_D),[5] Shear modulus (G), Young's modulus (E), and Bulk compressibility (β) can be evaluated:

$$\theta_D = \left(\frac{h}{k_B} \right) \left[\frac{9N}{4\pi V (V_L^{-3} + 2V_S^{-3})} \right]^{1/3} \tag{2.9}$$

$$G = dV_S^2 \tag{2.10}$$

$$E = G\left[\frac{3V_L^2 - 4V_S^2}{V_L^2 - V_S^2}\right] \tag{2.11}$$

and

$$\beta = \frac{1}{d\left(V_L^2 - \frac{3}{4}V_S^2\right)} \tag{2.12}$$

where, h is the Plank's constant, k_B is the Boltzmann constant, N is the number of atoms in a unit cell, V is the unit cell volume, and d is total density.

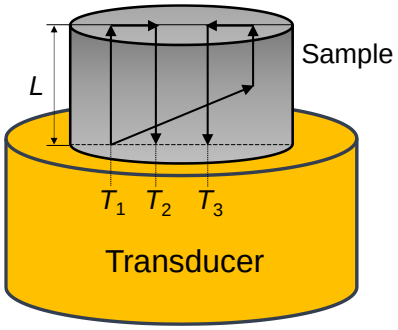

Figure 2.6 Schematic illustration of the sound velocity measurement.

2.5 Hall Measurements

Hall measurement was carried out by van der Pauw method as shown in Figure 2.7.[6] In general, an arbitrary shaped thin-plate sample is used, and must not contain holes, and nonconducting islands and inclusion. The sample shape was square (~8 x 8mm^2) with the thickness of ~1mm, and probes were contacted on four corners of the surface of the sample through ohmic contacts.

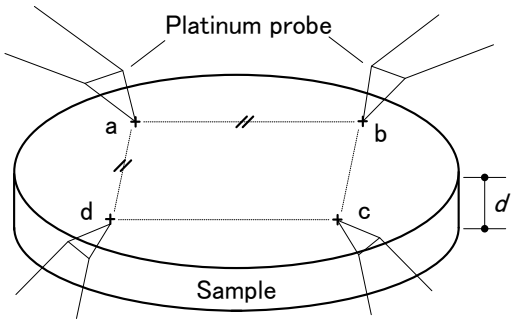

Figure 2.7 Schematic diagram of Van der Pauw's method.

The electrical resistivity (ρ) and sheet resistance R_{sheet} are calculated by the following equations:

$$\rho = \frac{\pi L_3}{\ln 2} \frac{R_a + R_b}{2} F \tag{2.13}$$

and

$$R_{sheet} = \frac{\rho}{L_3} \tag{2.14}$$

where, L_3 is the sample thickness, R_a and R_b are the averages of the opposite side resistances, and F is the balance factor, The F value can be regressively calculated from

$$\sinh\left(\frac{r_{ratio}-1\ln 2}{r_{ratio}+1F}\right)=\frac{1}{2}\exp\left(\frac{\ln 2}{F}\right),0\le F\le 1 \tag{2.15}$$

The r_{ratio} is equal to R_a/R_b. Then, the Hall coefficient R_H is given by

$$R_H=\frac{L_3}{B}\frac{V_H}{I_s}=\frac{L3}{B}\left|\frac{Rc+Rd}{2}\right| \tag{2.16}$$

where, V_H is the measured Hall voltage, B is the applied magnetic field, I_S is the electric current, and R_c and R_d are the averages of the Hall resistances for each electric current direction. The noise ratio N_{ratio} and direction dependence D_{ratio} are determined by the following equations:

$$N_{ratio}=\frac{2N_{cd}}{\left|R_c+R_d\right|}\times 100[\%] \tag{2.17}$$

and

$$D_{ratio}=\frac{\left|R_c-R_d\right|}{\left|R_c+R_d\right|}\times 100[\%] \tag{2.18}$$

where, N_{ratio} represents the root-mean-square deviation of $(R_c + R_d)/2$. D_{ratio} is the indicator to represent sample nonuniformity. In this study, the author used the measured R_H as the analytical data, if $N_{ratio} \le 3\%$ and $D_{ratio} \le 5\%$.

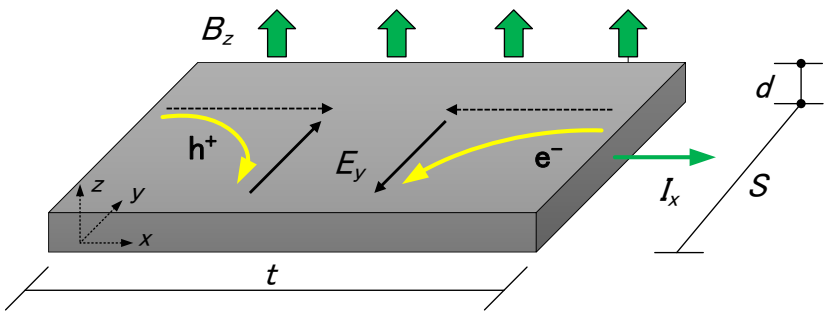

Figure 2.8 Schematic diagram of the Hall effect.

References

1) J. P. Eberhart, *Structural and Chemical Analysis of Materials* (Wiley, Chichester, U.K., 1991).
2) T.G. Rochow and P.A. Tucker: Introduction to Microscopy by Means of Light, Electrons, X Rays, or Acoustics Second Edition (Plenum Press, New York, 1994).
3) G. A. Slack, Solid State Phys. 34, 1 (1979).
4) S. Yamanaka, A. Kosuga, and K. Kurosaki, J. Alloys Comp. 350, 288 (2003).
5) H. Inaba and T. Yamamoto, Netsu Sokutei. 10, 132 (1983).
6) L. J. van der Pauw, Philips Tech. Rev. 20, 220 (1958).

CHAPTER III

Thermoelectric Properties of Indium-Filled Skutterudites $In_xCo_4Sb_{12}$

3.1 Introduction

Thermoelectric (TE) materials can be used for energy conversion from heat into electrical power. The efficiency of the energy conversion of TE materials is determined by the dimensionless figure of merit, $ZT = S^2T/\rho/\kappa$, where S is the Seebeck coefficient, T is the absolute temperature, ρ is the electrical resistivity, and κ is the total thermal conductivity ($\kappa = \kappa_{lat} + \kappa_{ele}$, where κ_{lat} and κ_{ele} are the lattice and electronic contributions, respectively).[1-3] The ZT value directly reflects the efficiency of the energy conversion; therefore, the development of high-ZT materials is the main goal in this research area. According to the equation for ZT, a large S, low ρ, and low κ are required to maximize ZT. These transport properties are interrelated with each other, so that optimization of these physical properties is required to maximize ZT.[2-3]

Skutterudite compounds are particularly promising candidates for advanced TE materials and have become a focus of lasting interest due to their highly tunable transport properties.[4] Skutterudite compounds have an MX_3 composition with the body-centered cubic structure, where M is a metal atom, such as Co, Rh, or Ir, and X represents a pnicogen atom, such as P, As, and Sb. There are two cages in each unit cell of the structure with sufficient size to accommodate metal atoms and form filled skutterudites. When a third atom is incorporated into the cage, the formula of the compounds becomes RM_4X_{12}, where R is the filling atom that is bonded weakly with the other atoms in the structure as shown in Figure 3.1. Cage-filling atoms can act as electron donors, so that filling of the cage with various atoms can lead to an optimum electron concentration. These filled atoms also act as phonon scattering

centers to significantly reduce κ_{lat}, which can result in improvement of the *ZT* for skutterudite compounds.[5-7)]

$CoSb_3$ is a typical skutterudite that has a very high power factor (S^2/ρ), but a κ_{lat} that is too high. Our group has recently reported the TE properties of Tl- and Ga-filled $CoSb_3$.[8-9)] The results indicate that as the filling ratio of Tl and Ga into $CoSb_3$ is increased, κ_{lat} is significantly decreased, which leads to improvement of the *ZT*. In particular, the *ZT* value for the Tl-filled system is enhanced up to 0.90 at 600 K. Thus, the motivation for this work is to further investigate the $CoSb_3$ system with In filling.

Various results on the TE properties of In-filled skutterudites have been reported, in which the In filling limit into $CoSb_3$ is closed to $x = 0.22$ in $In_xCo_4Sb_{12}$.[10-11)] In the present study, polycrystalline samples of $In_xCo_4Sb_{12}$ (x = 0.05, 0.10, 0.15, 0.20, 0.25, 0.30, 0.35, and 0.40) were prepared and their TE properties were examined from room temperature to 773 K. The filling limit of In into $CoSb_3$ cages was also investigated with respect to variation of the lattice parameter as a function of the In filling ratio of $In_xCo_4Sb_{12}$.

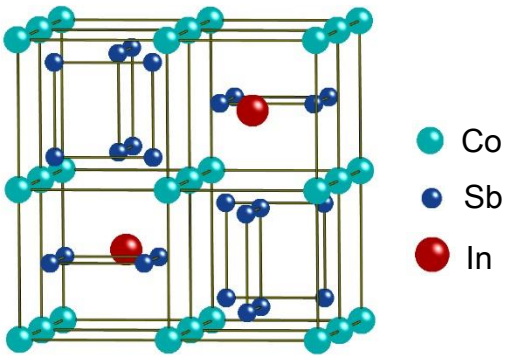

Figure 3.1 Crystal structure of $In_xCo_4Sb_{12}$ ($0.05 \leq x \leq 0.40$)

3.2 Experimental

In can be filled into the cages of the $CoSb_3$ structure up to around 22%, i.e., $x = 0.22$ in $In_xCo_4Sb_{12}$, and the highest *ZT* values are obtained after exceeding the filling limit.[10-11)] Therefore, the compositions prepared in the present study were

determined as $In_xCo_4Sb_{12}$ (x = 0.05, 0.10, 0.15, 0.20, 0.25, 0.30, 0.35, and 0.40). Polycrystalline samples were prepared from stoichiometric ratios of In (99.99%), Co (99%), and Sb (99.9%) chunks by direct reaction in a sealed silica tube. The silica tubes were heated slowly up to 1323 K and then annealed at 773 K for 1 week. The obtained ingots were crushed into fine powders, followed by hot-pressing in a graphite die at 923 K under a pressure of 50 MPa for 2 h in an Ar flow. Structural characterization was conducted using *X*-ray diffraction (XRD) analysis in air at room temperature with Cu Kα radiation. The microstructure was investigated by field emission scanning electron microscopy (FE-SEM; Jeol, JSM-6500F) with energy dispersive X-ray (EDX) analysis in vacuum at room temperature. Two polycrystalline samples were prepared for each composition; column-shaped samples (10 mm diameter, 15 mm thick) for S and ρ measurements, and disc-shaped samples (10 mm diameter, 1 mm thick) for thermal diffusivity (α) measurements. S and the ρ were measured using a commercially available apparatus (Ulvac, ZEM-1) in a He atmosphere. α was measured by the laser flash method in a vacuum using a commercially-available thermal constant analyzer (Ulvac TC-7000). κ was evaluated via the standard equation of $\kappa = \alpha C_p d$, where C_p and d are heat capacity and density, respectively. C_p was estimated using the Dulong-Petit model, i.e., $C_p = 3R$, where R is the gas constant. The densities of the bulk samples were calculated on the basis of the measured weight and dimensions. All TE properties were measured from room temperature to 773 K.

3.3 Results and discussion

The powder XRD patterns of the polycrystalline samples of $In_xCo_4Sb_{12}$ (x = 0.10, 0.20, 0.30, and 0.40) are shown in Figure 3.2, together with the literature data for $CoSb_3$.[12] Almost all the peaks in the XRD patterns were identified as peaks derived from the skutterudite phase. A negligible peak for $CoSb_2$ as an impurity phase was observed in the x = 0.30 sample pattern. In addition, a peak corresponding to InSb was observed in all XRD patterns of the samples.

The lattice parameters calculated from the XRD patterns of $In_xCo_4Sb_{12}$ (x = 0.05, 0.10, 0.15, 0.20, 0.25, and 0.30) are plotted in Figure 3.3, together with the data of polycrystalline samples of $Tl_xCo_4Sb_{12}$ and $Ga_xCo_4Sb_{12}$ for comparison.[8-9] The lattice parameters of $In_xCo_4Sb_{12}$ increased linearly with In-addition up to around x = 0.10, after which they remained almost constant. In contrast, for $Tl_xCo_4Sb_{12}$ and $Ga_xCo_4Sb_{12}$, the lattice parameters increased linearly up to around x = 0.20 and 0.05, respectively.[8-9] Therefore, the maximum filling limits of Ga, In, and Tl into the cages of $CoSb_3$ were confirmed to be different, even these are all group 13 elements. Relatively high densities were obtained for all samples, and these are summarized in Table 3.1 together with the lattice parameters.

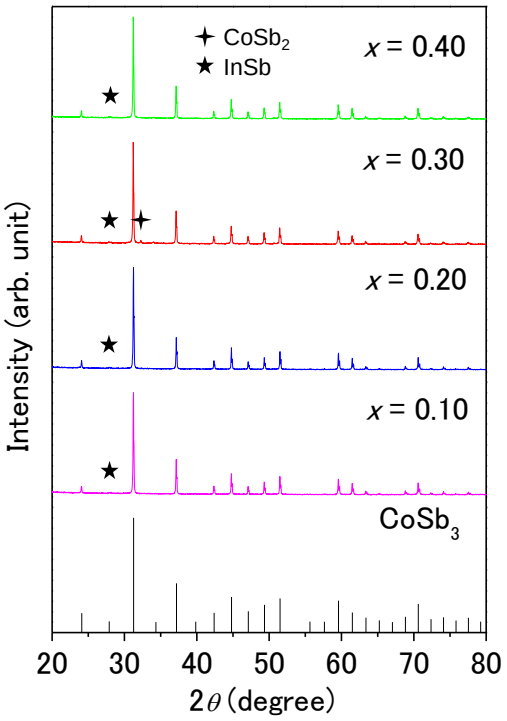

Figure 3.2 Powder XRD patterns of $In_xCo_4Sb_{12}$ (x = 0.10, 0.20, 0.30, and 0.40) polycrystalline samples, together with the literature data for $CoSb_3$.[12]

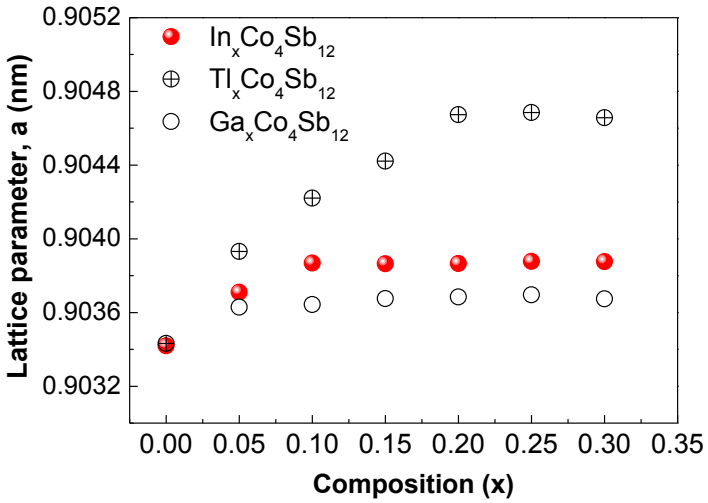

Figure 3.3 Lattice parameters of $In_xCo_4Sb_{12}$ (x = 0.05 ~ 0.30) polycrystalline samples, together with the data for $Tl_xCo_4Sb_{12}$ and $Ga_xCo_4Sb_{12}$.[8, 9)]

Table 3.1 Lattice parameters a, and densities d, of InxCo4Sb12 (x = 0.05 ~ 0.40) polycrystalline samples (T.D: theoretical density)

x	a (nm)	d (g cm^{-3})	%T.D.
0.05	0.90371	7.64	99.7
0.10	0.90387	7.64	99.5
0.15	0.90386	7.61	98.7
0.20	0.90387	7.64	98.8
0.25	0.90388	7.76	97.8
0.30	0.90388	7.63	98.1
0.35	0.90388	7.53	96.5
0.40	0.90388	7.56	96.5

Figures 3.4(a) and (b) show the SEM and EDX mapping images for the samples of $In_{0.05}Co_4Sb_{12}$ and $In_{0.10}Co_4Sb_{12}$, respectively. The surface of the $In_{0.05}Co_4Sb_{12}$ sample was homogeneous with no significant evidence of secondary phases by EDX analysis, as indicated in Figure 3.4(a). On the other hand, the surface

of the $In_{0.10}Co_4Sb_{12}$ sample was inhomogeneous. The In-rich regions were clearly observed in Figure 3.4(b).

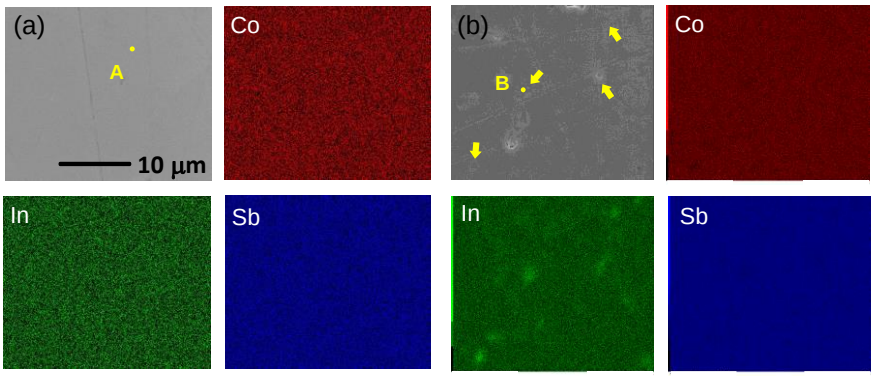

Figure 3.4 FEM and EDX mapping images of hot-pressed samples of (a) $In_{0.05}Co_4Sb_{12}$ and (b) $In_{0.10}Co_4Sb_{12}$.

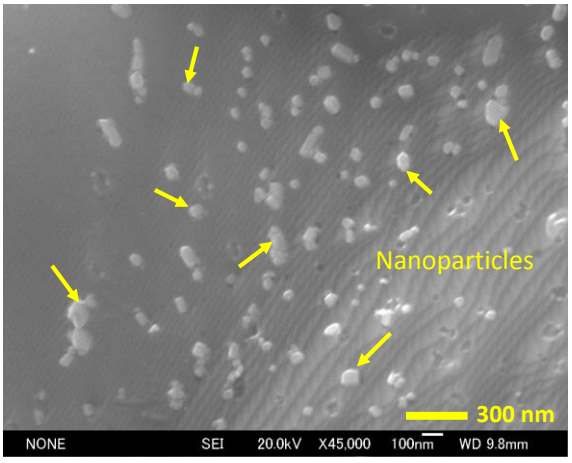

Figure 3.5 FE-SEM images of fracture surface of $In_{0.35}Co_4Sb_{12}$.

The chemical compositions at points A and B shown in the SEM images are summarized in Table 3.2. It was confirmed that the matrix phase of the $In_{0.05}Co_4Sb_{12}$ sample (shown as point A in Figure 3.4 (a)) and the impurity phase of the $In_{0.10}Co_4Sb_{12}$ sample (shown as point B in Figure 3.4 (b)) are mainly composed of

$CoSb_3$ and InSb, respectively. It was previously reported that the filling limit of In into the $CoSb_3$ cages in $In_xCo_4Sb_{12}$ was around x = 0.22.[9-10] The reason for the discrepancy in the filling limit is yet to be determined.

Figure 3.5 shows the fracture surface FE-SEM image of $In_{0.35}Co_4Sb_{12}$. The nanoparticles with sizes of tens of nanometers to 100 nm were observed in the grain boundaries. However, the chemical composition can not be detected due to the nanoscale is beyond the EDX detection limit. However, according to the previous literatures, In and Ga are known as easily to form nanoparticles when they were over added in skutterudites. And the nanoparticles have the chemical composition of MSb (M = In or Ga).[13,14] The appearance of InSb nanoinclusions has been explained by in situ formation due to diffusion of filler atoms out of the icosahedral voids of the metastable $In_xCo_4Sb_{12}$ skutterudites.[15] This hypothesis on the metastability of $In_xCo_4Sb_{12}$ is also supported by the zero-filling-fraction calculated for the solubility of In in $CoSb_3$ and by calculations of the Gibbs free energy, which remains positive over the whole temperature range.[16] And consider the melting point of InSb is 790 K, therefore, the final formation of InSb is happened on the temperature decreasing step of sintering.

Table 3.2 Chemical compositions of points A and B (at. %) determined by EDX point analysis.

	A	**B**
Co	23.6	1.4
In	0.3	46.6
Sb	76.1	52.0

The temperature dependence of the electrical conductivity ($\sigma = 1/\rho$) and the Seebeck coefficient (S) of the $In_xCo_4Sb_{12}$ (x = 0.05, 0.10, 0.15, 0.20, 0.25, 0.30, 0.35, and 0.40) polycrystalline samples are shown in Figures 3.6 (a) and (b), respectively. σ for all of the samples decreased with increasing temperature, which is consistent

with other In-filled skutterudites known as typical, heavily doped, band-conducting semiconductors reported by Mallik et al.[17)]

S was negative for all the samples, which indicates that the majority charge carrier was electrons. Thus, all samples are *n*-type semiconductors from room temperature to 773 K. Figure 3.6(a) shows that σ generally increased with increase in the In content. In contrast, the absolute *S* values decreased with the increasitheng In content, as shown in Figure 3.6(b). Moreover, the temperature dependence of *S* for the heavily In-added $CoSb_3$ samples was rather flat. These results suggest that In addition into $CoSb_3$ results in the supply of electrons, so that the carrier concentration increases. In addition, the change in both σ and *S* with an increase in the In content was not coincident, which may be due to the influence of impurities such as InSb and $CoSb_2$ that are formed after the maximum filling limit of In into $CoSb_3$ is exceeded.

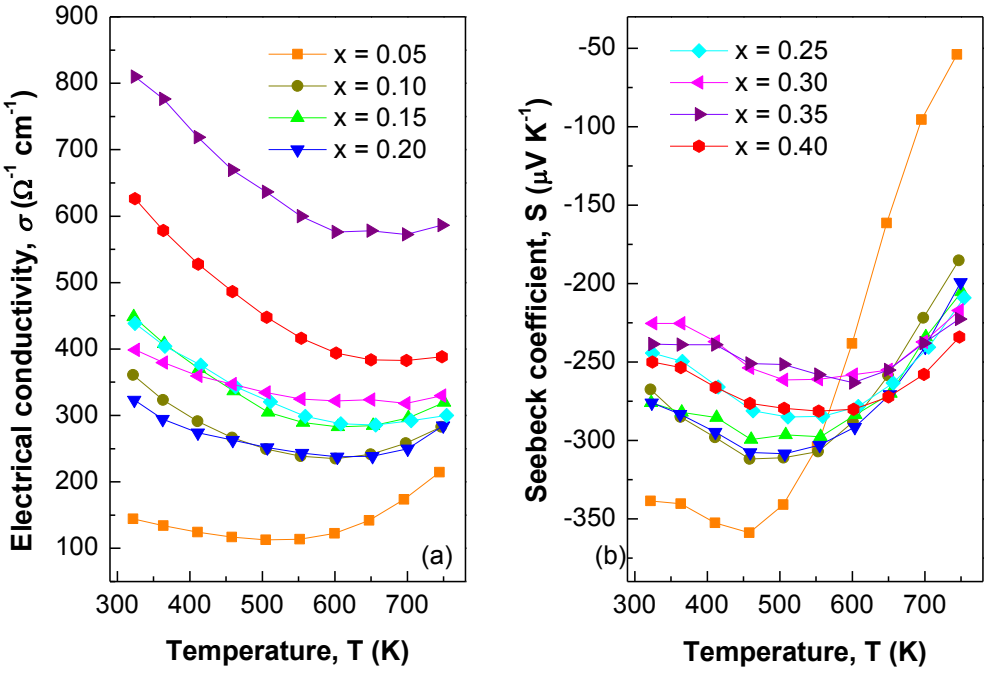

Figure 3.6 Temperature dependence of (a) electrical conductivity σ and (b) Seebeck coefficient *S* for $In_xCo_4Sb_{12}$ (x = 0.05 ~ 0.40) polycrystalline samples.

Figure 3.7(a) shows the thermal conductivity (κ) of $In_xCo_4Sb_{12}$ (x = 0.05, 0.10, 0.15, 0.20, 0.25, 0.30, 0.35, and 0.40) as a function of temperature. κ decreased with increasing temperature and then increased with the temperature at around 550 K. This temperature dependence can be attributed to the bipolar conduction in semiconductors, where the charge carriers are thermally excited, and hence, the bipolar contribution is supplemented by a strong additional term for the thermal transport. κ decreases with an increase in the In content, which is quite different from that previously reported in Refs. 10 and 11, in which κ increased with increase in the In content.

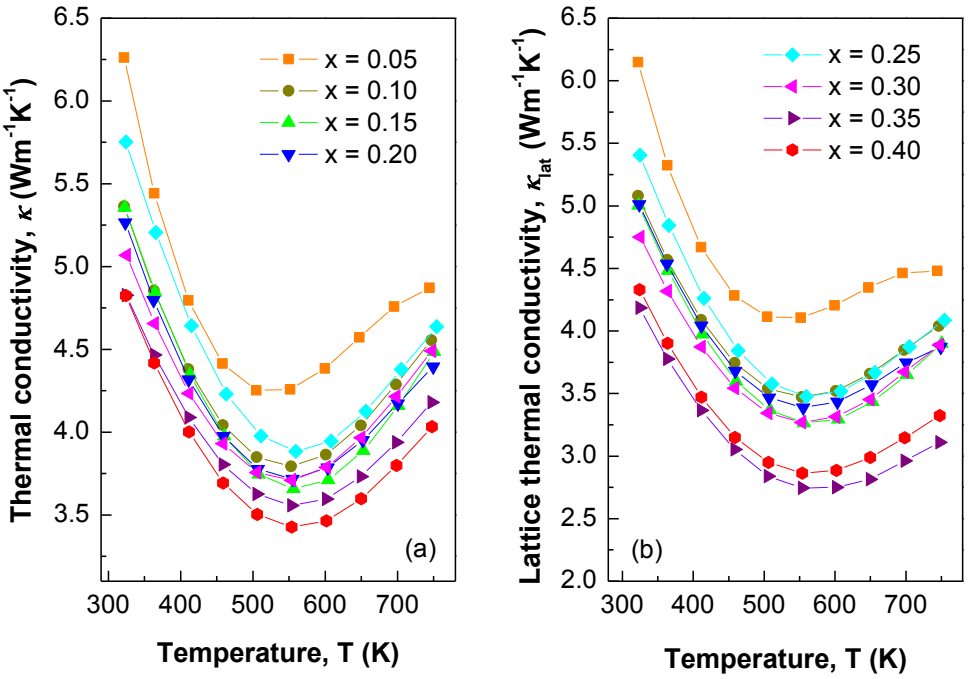

Figure 3.7 Temperature dependence of (a) thermal conductivity κ and (b) lattice thermal conductivity κ_{lat} for $In_xCo_4Sb_{12}$ (x = 0.05 ~ 0.40) polycrystalline samples.

The lattice thermal conductivity (κ_{lat}) was obtained by subtraction of $\kappa_{el} = L\sigma T$ (where L is the Lorenz number = 2.45×10^{-8} $W\Omega K^{-2}$) from the measured κ, i.e., $\kappa_{lat} = \kappa - L\sigma T$. Figure 3.7(b) shows that κ_{lat} for $In_xCo_4Sb_{12}$ (x = 0.05, 0.10, 0.15, 0.20, 0.25, 0.30, 0.35, and 0.40) decreased with In-addition, which is probably due to phonon scattering by both In rattling within the cages and impurities present in the samples. Consider the mean free path of phonons in $CoSb_3$ was estimated to around 85 nm, [18] therefore, the nanoparticles with sizes smaller than 85 nm would effectively scatter heat carrying phonons. However, as mentioned above, the κ_{lat} was reduced by the combined effects of several factors. Thus, it is difficult to evaluate the nanoparticle effect on κ_{lat} quantitatively. The $In_{0.35}Co_4Sb_{12}$ compound exhibited the lowest value of κ_{lat} (2.86 Wm^{-1} K^{-1} at 550 K).

The temperature dependence of ZT for $In_xCo_4Sb_{12}$ (x = 0.05, 0.10, 0.15, 0.20, 0.25, 0.30, 0.35, and 0.40) is shown in Figure 3.8. Although In could be filled into $CoSb_3$ cages in $In_xCo_4Sb_{12}$ only in the range of $0.05 < x < 0.10$, a significant reduction of κ_{lat} was achieved, which led to an enhancement of ZT. The ZT values generally increased with increasing In content, and a maximum ZT value of 0.67 was obtained for the $In_{0.35}Co_4Sb_{12}$ composition at 600 K.

After exceeding the filling limit of In into $CoSb_3$, InSb exists in the samples as the main impurity phase, which leads to the formation of Sb vacancy in the skutterudite phase. Therefore, it is important to consider the effect of the Sb vacancy on the TE properties of the sample. Formation of the Sb vacancy in the skutterudite phase is helpful for reduction of the κ_{lat} by phonon scattering, while the vacancy would also scatter carriers which results in the reduction of the carrier mobility. On the other hand, as for the impact of InSb on the TE properties, it has been reported that when the size of the InSb phase is nanoscale, existing of the InSb phase is good for enhancement of the TE properties.[19] Therefore, in the present study, existing of the InSb phase would lead to the reduction of both the κ_{lat} and carrier mobility. As for the impact of In filling on the TE properties, it can be said that the In atoms filled in the cages of the $CoSb_3$ crystal act as phonon scattering centers, leading to significant reduction of the κ_{lat}. In order to understand the impacts of the InSb phase, Sb

vacancy, and filled In on the TE properties of $CoSb_3$, the authors have a plan to perform further experiments such as Hall effect measurements on the samples to evaluate the carrier mobility.

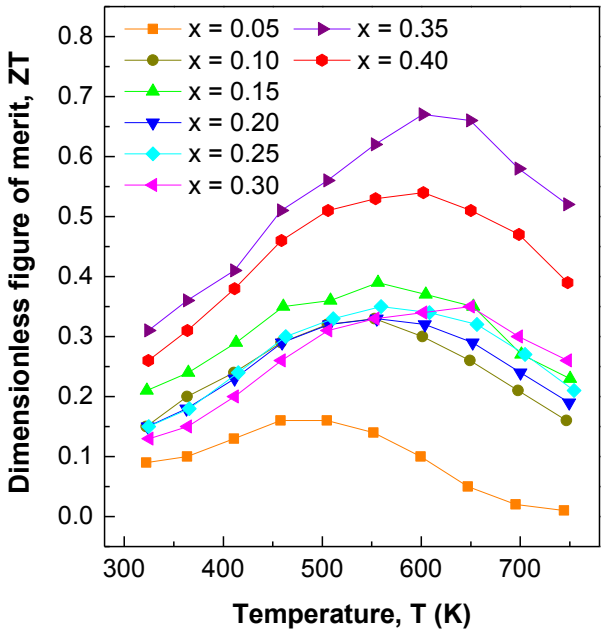

Figure 3.8 Temperature dependence of the dimensionless figure of merit *ZT*, for polycrystalline samples of $In_xCo_4Sb_{12}$ (x = 0.05 ~ 0.40).

3.4 Summary

In the present study, polycrystalline samples of In-added $CoSb_3$ with compositions of $In_xCo_4Sb_{12}$ (x = 0.05, 0.10, 0.15, 0.20, 0.25, 0.30, 0.35, and 0.40) were prepared and the TE properties were investigated from room temperature to 773 K. In could be filled in $In_xCo_4Sb_{12}$ only in the range of $0.05 < x < 0.10$, and when the filling limit was exceeded, InSb and $CoSb_2$ secondary phases were formed in the samples. All samples exhibited negative S values. In-adding into $CoSb_3$ slightly reduced the absolute value of S, but increased σ and reduced κ_{lat}. In contrast with the Tl-filled skutterudite system,[8] the filling limit of In is too low, which results in

insufficient doping and thus the phonon scattering effect by In rattling within the cage should be weak. However, impurities such as InSb, formed after exceeding the filling limit of In into $CoSb_3$, had a significant role in reducing κ_{lat} and thereby enhancing *ZT*. Further study will be aimed at increasing the filling limit of an In-filled skutterudite system or a double-filling or multi-filling approach to enhance *ZT*.

References

1) G.A. Slack, CRC Handbook of Thermoelectrics, E.d. D.M. Rowe (Boca Raton, FL: CRC Press, 1995), p. 407-440.
2) G.S. Nolas, J. Sharp, and H.J. Goldsmid, Thermoelectrics: Basic principles and New Materials Developments (Berlin: Springer, 2001).
3) A.F. Ioffe, Semiconductor Thermoelements and Thermoelectric Cooling (London: Infosearch Limited, 1957).
4) B.C. Sales, D. Mandrus, and R.K. Williams, Science **272**, 1325 (1996).
5) D.T. Morelli, and G.P. Meisner, J. Appl. Phys. **77**, 3777 (1995).
6) X.Y. Zhao, X. Shi, L.D. Chen, W.Q. Zhang, W.B. Zhang, and Y.Z. Pei, J. Appl. Phys. **99**, 053711 (2006).
7) Z. Zhou, C. Uher, A. Jewell, and T. Caillat, Phys. Rev. B **71**, 235209 (2005).
8) A. Harnwunggmoung, K. Kurosaki, H. Muta, and S. Yamanaka, Appl. Phys. Lett. **96**, 202107 (2010).
9) A. Harnwunggmoung, K. Kurosaki, T. Plirdpring, T. Sugahara, Y. Ohishi, H. Muta, and S. Yamanaka, J. Appl. Phys. **110**, 013521 (2011).
10) T. He, J. Chen, H.D. Rosenfeld, and M.A. Subramanian, Chem. Mater. **18**, 759 (2006).
11) R.C. Mallik, C. Stiewe, G. Karpinski, R. Hassdorf, and E. Muller, J. Electron. Mater. **38**, 7 (2009).
12) Z. Wegrzyn, A. Malecki, M. Bucko, and K.T. Wojciechowski, J. Appl. Crystallogr. **18**, 46 (2001).
13) H. Li, X. Tang, Q. Zhang, and C. Uher, Appl. Phys. Lett. **94**, 102114 (2009).
14) X. Su, H. Li, Y. Yan, H. Chi, X. Tang, Q. Zhang, and C. Uher, J. Mater. Chem. **22**, 15628 (2012).
15) J. Eilertsen, S. Rouvimov, and M. A. Subramanian, Acta Mater. **60**, 2178 (2012).
16) X. Shi, W. Zhang, L.D. Chen, and J. Yang, Phys. Rev. Lett. **95**, 185503 (2005).
17) R.C. Mallik, C. Stiewe, G. Karpinski, R. Hassdorf, and E. Muller, Proc. 6th European Conf. on Thermoelectrics (ETC-2008), Paris, France, P1-25-1-5 (2008).
18) D.W. Song, W.L. Liu, T. Zeng, T. Borca-Tasciuc, G. Chen, J.C. Caylor, T.D. Sands, Appl, Phys. Lett. **77**, 3854 (2000).

19) H. Li, X. Tang, Q. Zhang, and C. Uher, Appl. Phys. Lett. **94**, 102114 (2009).

CHAPTER IV

Thermoelectric Properties of Group 13 Elements Triple-Filled Skutterudites: Nominal $In_xGa_{0.02}Tl_{0.20}Co_4Sb_{12}$

4.1 Introduction

Thermoelectric (TE) materials can be used for direct energy conversion from waste heat into electrical power, and have the merit of no moving parts and high reliability. The efficiency of the energy conversion of TE materials is governed by the dimensionless figure of merit, $ZT = S^2T/\rho/\kappa$. In this equation, S is the Seebeck coefficient, T is the absolute temperature, ρ is the electrical resistivity, and κ is the total thermal conductivity ($\kappa = \kappa_{lat} + \kappa_{el}$, where κ_{lat} and κ_{el} are the lattice and electronic contributions, respectively) 1). Owing to the ZT value directly reflects the efficiency of the energy conversion, the development of high-ZT materials has a significant meaning for more effective energy savings by recycling the waste heat. To achieve high ZT, a large S, low ρ, and low κ are required, however, S, ρ, and κ_{el} are strongly interrelated with each other in materials, so reduction of κ_{lat} is required to maximize ZT.[2, 3)]

Skutterudite compounds are particularly promising candidates for advanced TE materials and have become a focus of lasting interest due to the high carrier mobility and the reasonable band gap.[4)] Binary skutterudite compounds have an MX_3 (M = Co, Rh, or Ir; X = P, As, or Sb) composition with body-centered cubic structure. There are two cages in each unit cell of the structure with sufficient size to accommodate a large range of atoms with different sizes to form so called filled skutterudites.[5)] The cage-filling atoms act as electron donors, so that filling of the cages with various atoms can lead to an optimum electron concentration to maximize the power factor (S^2/ρ). In addition, the filler atoms are bound weakly with the host atoms and rattle, resulted in acting as phonon scattering centers to reduce κ_{lat}

significantly.[6, 7] Therefore, it is possible to reach a maximized *ZT* by separate optimization of electrical and thermal transports properties in skutterudites.

It has been widely studied that the cages in $CoSb_3$ can be fully or partially filled with a variety of different atoms, including alkali metals (Li, Na, and K),[8-10] alkaline earth elements (Ca, Sr, and Ba),[11-13] and rare-earth elements (La, Ce, Yb, Eu, Nd, and Sm).[14-19] Recently, skutterudites filled by group 13 elements (Ga, In, and Tl) have attracted much attention as high-performance TE materials.[20-22] It has been reported that the group 13 elements can exist not only in the void, but also at the Sb and Co sites.[23] Our group also has studied the TE properties of Ga-, In-, and Tl- filled skutterudites and confirmed that the group 13 elements filled-skutterudites exhibit low κ_{lat} and thereby relatively high *ZT* values.[24-26] In particular, the maximum values of *ZT* of 0.9 and 0.7 at 600 K have been obtained for Tl- and In-filled skutterudites, respectively.[25, 26] In addition, to the single element filled-skutterudites, the TE properties of In and Tl double filled skutterudites have been examined in our group. Owing to the further reduction of κ_{lat} by effective phonon scattering induced both by the rattling of In and Tl as well as by In_2O_3 nano-precipitates, the *ZT* was enhanced and the maximum *ZT* value of 1.2 was obtained at 700 K.[27]

On the other hand, the TE properties of triple elements filled skutterudites have been studied recently.[28-30] It is considered that phonons with different frequencies are scattered by various vibration modes induced by rattling of different filler atoms within the cages. Therefore, the triple-filling is one of the effective methods for further reduction of κ_{lat}. However, there are no reports on the TE properties of group 13 elements triple filled skutterudites so far. Therefore, in the present study, the polycrystalline samples of group 13 elements triple filled skutterudites were prepared and their TE properties were investigated from room temperature to 773 K.

The sample compositions were set as $In_xGa_{0.02}Tl_{0.20}Co_4Sb_{12}$ ($0 \leq x \leq 0.30$), because the maximum filling limit of Ga, In, and Tl in Co_4Sb_{12} are reported to be x = 0.02 in $Ga_xCo_4Sb_{12}$, x = 0.08 in $In_xCo_4Sb_{12}$, and x = 0.22 in $Tl_xCo_4Sb_{12}$, respectively.[22, 24-26] In the present case, we expected that Ga and Tl are fully filled and with

increasing In content the κ_{lat} can be significantly reduced by triple filling as well as nano-inclusions formed after exceeding the filling limit of In.[31, 32)]

4.2 Experimental

The triple filled skutterudites: $In_xGa_{0.02}Tl_{0.20}Co_4Sb_{12}$ ($0 \leq x \leq 0.30$) were synthesized by a combination method of traditional melting and long-term high-temperature annealing. The appropriate amounts of elemental metal chunks of In, Ga, Tl, Co, and Sb were weighted and put in silica tubes in a glove-box under an Ar flow atmosphere. The silica tubes were sealed under vacuum. The sealed silica tubes were heated slowly up to 1323 K and then annealed at 973 K for 10 days. The obtained ingots were crushed into powders, followed by hot-pressing in a graphite die at 923 K under a pressure of 50 MPa for 2 h in an Ar flow atmosphere.

Structural characterization was conducted using X-ray diffraction (XRD) analysis in air at room temperature with Cu Kα radiation. The microstructure and chemical composition of the samples were investigated by field emission scanning electron microscopy (FE-SEM; JEOL JSM-6500F) with energy dispersive X-ray (EDX) analysis in vacuum at room temperature. S and ρ were measured using a commercially available apparatus (ULVAC, ZEM-1) in a He atmosphere. Thermal diffusivity (α) was measured by the laser flash method in a vacuum using a commercially-available thermal constant analyzer (ULVAC TC-7000). κ was evaluated via the standard equation of $\kappa = \alpha C_p d$, where C_p and d are heat capacity and density, respectively. C_p was estimated using the Dulong-Petit model, i.e., $C_p = 3nR$, where n is the number of atoms per formula unit and R is the gas constant. All TE properties were measured from room temperature to 773 K.

Hall coefficient (R_H) was measured at room temperature by the van der Pauw method under vacuum with an applied magnetic field of 0.5 T. The Hall carrier concentration (n_H) and Hall mobility (μ_H) were calculated from R_H assuming a single band model and a Hall factor of 1, i.e., $n_H = 1/(eR_H)$ and $\mu_H = R_H/\rho$, where e is the

elementary electric charge. The density of bulk samples was calculated on the basis of the samples' weight and dimensions.

4.3 Results and discussion

The powder XRD patterns of the samples are shown in Figure 4.1. Almost all the peaks in the XRD patterns were identified as peaks derived from the skutterudite phase, however a negligible $CoSb_2$ peak was observed in all of the samples. The lattice parameters of the skutterudite phase calculated from the XRD patterns are shown in Figure 4.2. The lattice parameter values were almost the same independent of the In content.

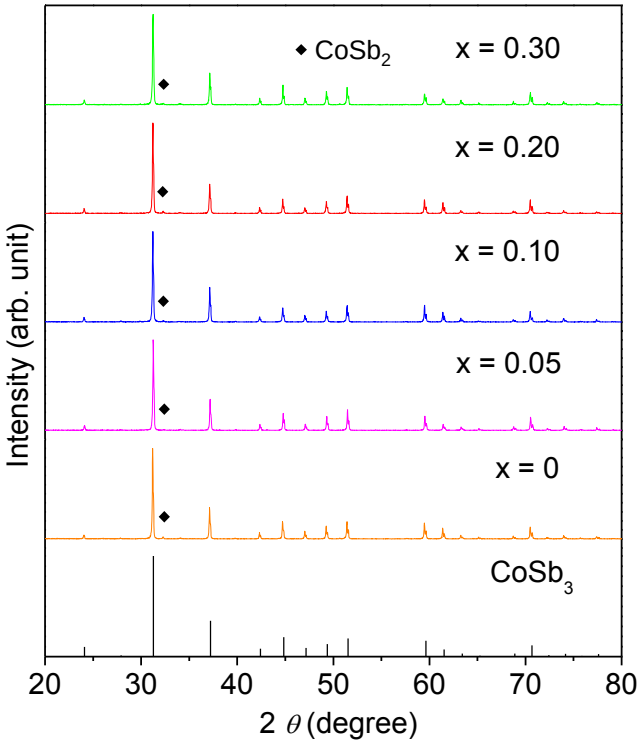

Figure 4.1 Powder XRD patterns of $In_xGa_{0.02}Tl_{0.20}Co_4Sb_{12}$ ($0 \leq x \leq 0.30$) polycrystalline samples.

Figure 4.3 shows the FE-SEM and EDX mapping images of the $In_{0.10}Ga_{0.02}Tl_{0.20}Co_4Sb_{12}$ sample. The chemical compositions of points A, B, and C were determined by the quantitative EDX point analysis, and the obtained data are summarized in Table 4.1. Although, the amounts of the filler elements did not exceed their respective filling limit, small amounts of Ga, In, and Tl were detected as the metal state (point A). In addition, precipitates of Tl_7Sb_2 and InSb were also observed (points B and C, respectively). As for other samples, the FE-SEM and EDX analyses were also carried out, and the same results as those of the $In_{0.10}Ga_{0.02}Tl_{0.20}Co_4Sb_{12}$ sample were obtained.

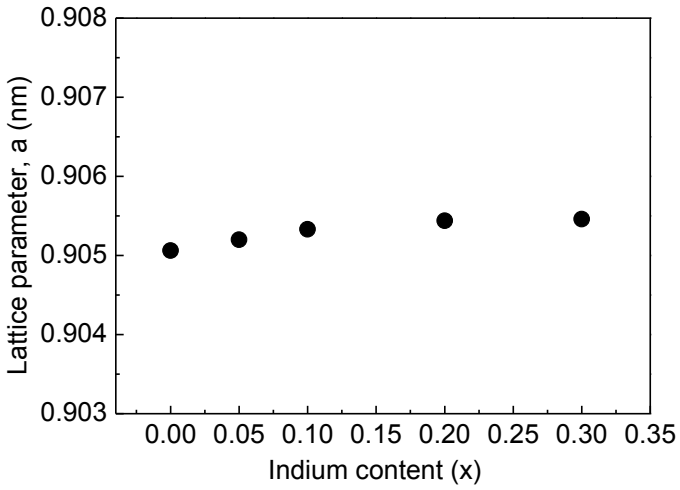

Figure 4.2 Lattice parameters of $In_xGa_{0.02}Tl_{0.20}Co_4Sb_{12}$ ($0 \leq x \leq 0.30$) polycrystalline samples

Since a very small amount of Ga was added, the Ga content in the skutterudite matrix phase was below the EDX detection limit. In addition, since the EDX peak positions of In and Sb are close to each other, the In content in the skutterudite matrix phase was not estimated accurately. Therefore, we assumed that the total filling fraction i.e. x in $(Ga, In, Tl)_xCo_4Sb_{12}$ was 0.22 and the In content was estimated by subtracting the Tl content from the total filling fraction. The amounts of group 13

elements in the skutterudite phase obtained in this manner are summarized in Table 2. It can be seen that the Tl content in the skutterudite phase decreased but the In content increased. This trend is well consistent with the previous results, that is, the filling fraction of one element decreases linearly whereas the other element's increases.[33] Since, the ionic radius of In^{+3} (81 pm) [34] is much smaller than that of Tl^{+1} (115 pm), [31] the lattice parameter should decrease with increasing the In content and with decreasing the Tl content in the skutterudite phase. However, as mentioned above, the lattice parameters of the skutterudite phase were almost the same independent of the In content. Therefore, the valence value of In in the present case would be close to 1+ (the ionic radius of In^{+1} is 104 pm[34]), not 3+, which is well consistent with the recent reports[35], in which it has been reported the valence state of In in the skutterudite structure is not 3+ but 1+.

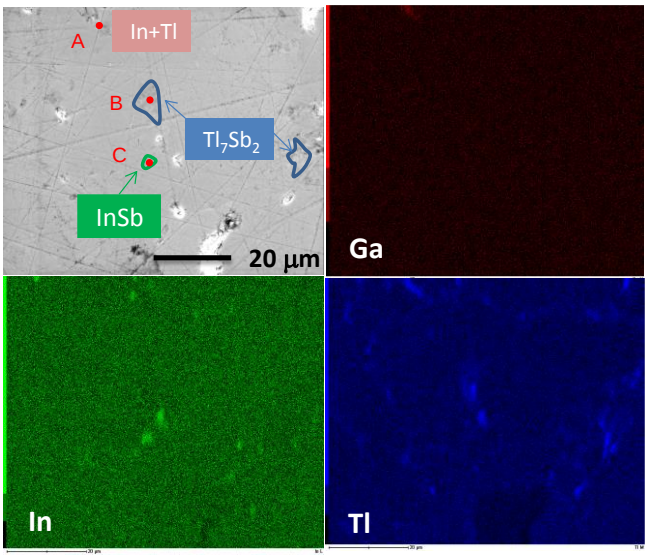

Figure 4.3 FE-SEM and mapping images of $In_{0.10}Ga_{0.02}Tl_{0.20}Co_4Sb_{12}$

Figure 4.4 shows the fracture surface images of $Ga_{0.02}Tl_{0.20}Co_4Sb_{12}$. The nano particles with size of 200 nm were observed in the grain boundaries by FE-SEM analysis. Figure 4.5 shows the fracture surface images of samples of $In_xGa_{0.02}Tl_{0.20}Co_4Sb_{12}$ (x = 0.05 ~ 0.30). The nano particles with distributed sizes of

20~200 nm were observed in all of the samples. In order to identify the chemical composition of the nano particles, we conducted EDX elemental analysis for the sample of $In_{0.20}Ga_{0.02}Tl_{0.20}Co_4Sb_{12}$, and the results as shown in Figure 4.6. All the mapping images show homogeneous matrix phase, no impurity phases were detected by EDX analysis. It can be considered that the nanoscale is beyond the EDX detection limit. However, according to the previous literature the chemical compositions of nanoparticles can be expected as InSb and GaSb as mentioned in chapter III.

Table 4.1 Chemical compositions of points A, B and C (at. %) in the sample of $In_{0.10}Ga_{0.02}Tl_{0.20}Co_4Sb_{12}$ determined by EDX point analysis

	A	B	C
Ga	3	0	0
In	48	6	42
Tl	43	70	9
Co	3	5	10
Sb	3	19	39
Chemical Composition	In+Tl metal	Tl_7Sb_2	InSb

Table 4.2 Ratio of fillers in the matrix of $In_xGa_{0.02}Tl_{0.20}Co_4Sb_{12}$ ($0 \leq x \leq 0.30$)

x	Ga*	:	Tl	:	In
0	-		0.20		0
0.05	-		0.18		0.04
0.10	-		0.16		0.06
0.20	-		0.16		0.06
0.30	-		0.13		0.09

*The amounts of Ga was below the EDX detection limit

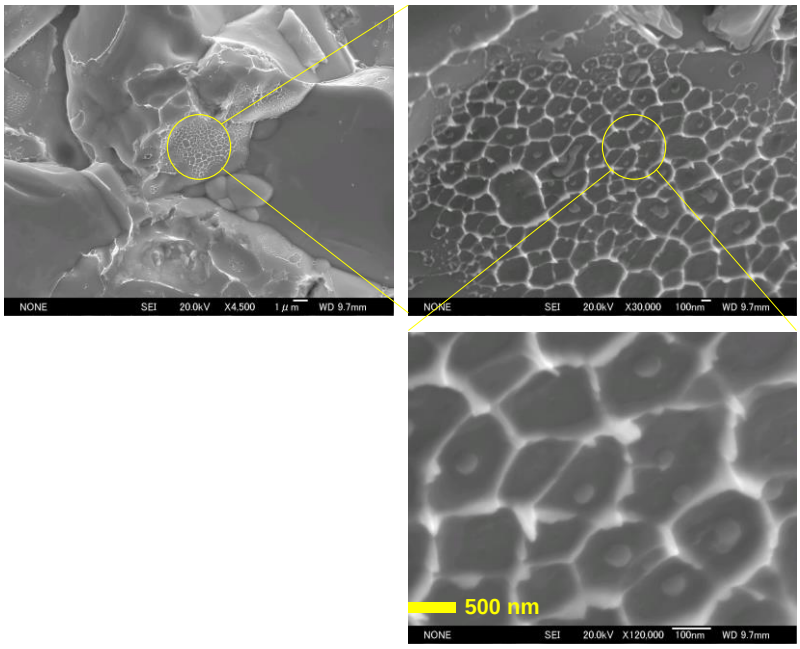

Figure 4.4 Fracture surface FE-SEM images of $Ga_{0.02}Tl_{0.20}Co_4Sb_{12}$

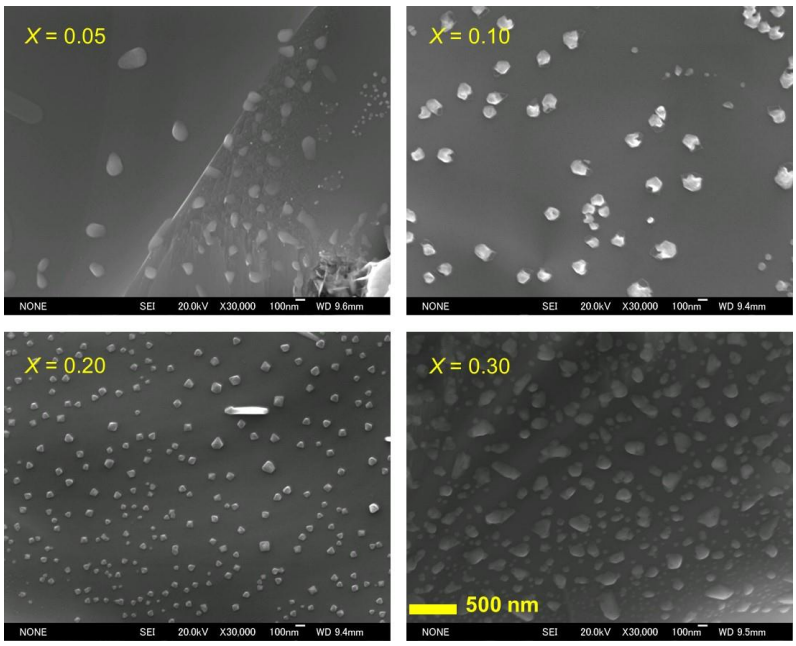

Figure 4.5 Fracture surface FE-SEM images of $In_xGa_{0.02}Tl_{0.20}Co_4Sb_{12}$ (x = 0.05 ~ 0.30)

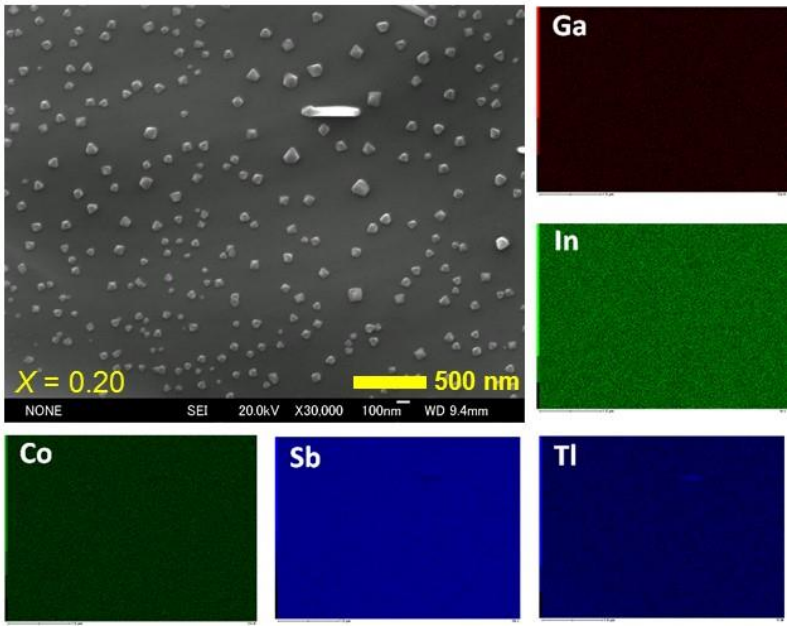

Figure 4.6 Fracture surface FE-SEM and mapping images of $In_{0.20}Ga_{0.02}Tl_{0.20}Co_4Sb_{12}$.

Table 4.3 Hall carrier concentration n_H (300 K), Hall mobility μ_H (300 K), and relative density for polycrystalline samples of $In_xGa_{0.02}Tl_{0.20}Co_4Sb_{12}$ ($0 \leq x \leq 0.30$)

x	n_H (10^{20} cm^{-3})	μ_H ($cm^2V^{-1}s^{-1}$)	%T.D.
0	2.54	31.1	96%
0.05	2.48	33.2	98%
0.10	2.81	30.6	99%
0.20	2.83	32.6	99%
0.30	2.92	29.2	98%

The carrier concentration (n_H) and the carrier mobility (μ_H) are summarized in Table 4.3. Both of n_H and μ_H did not change obviously. The n_H values slightly increased with increasing the In content. The filling fraction and the valence state of filler elements are the two main factors to determine the n_H. Although Tl donates one electron in $CoSb_3$,[20] i.e. Tl acts as Tl^{1+} in the skutterudite structure, the valence state of In is not clearly confirmed.[35-37] In the present case, it can be said that the valence

value of In in $CoSb_3$ is close to +1, not +3, because the n_H values are almost the same. This result is well consistent with the result derived from the lattice parameter shown above. All samples showed the relatively high density (96~99% of the theoretical density) as summarized in Table 4.3.

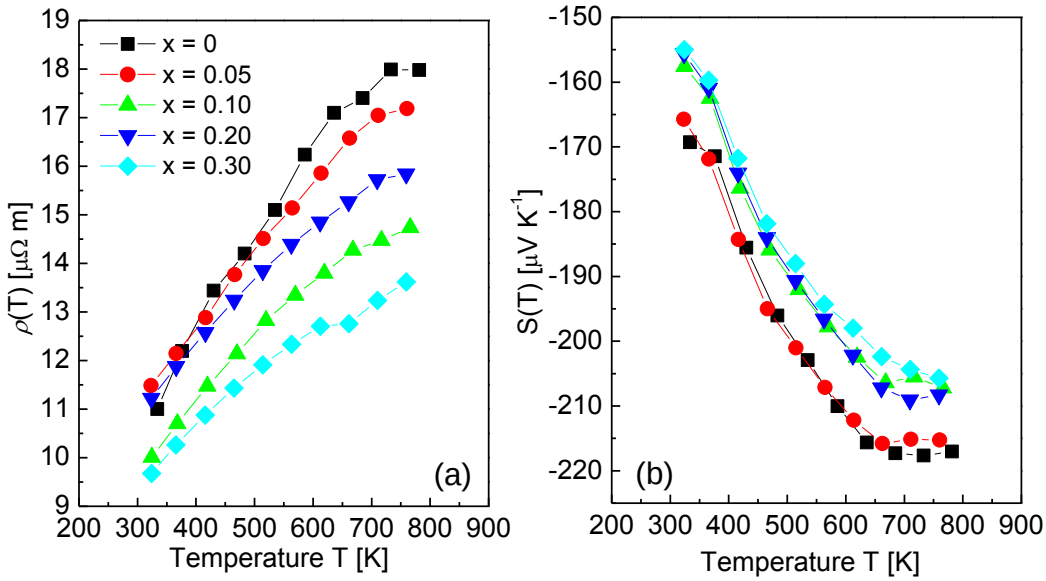

Figure 4.7 Temperature dependence of (a) electrical resistivity ρ, and (b) Seebeck coefficient S, for $In_xGa_{0.02}Tl_{0.20}Co_4Sb_{12}$ ($0 \le x \le 0.30$) polycrystalline samples.

The temperature dependences of the electrical resistivity (ρ), Seebeck coefficient (S), thermal conductivity (κ), and lattice thermal conductivity (κ_{lat}) of the $In_xGa_{0.02}Tl_{0.20}Co_4Sb_{12}$ ($0 \le x \le 0.30$) samples are shown in Figures 4.7(a) and (b) respectively. ρ for all of the samples increased with increasing temperature, showing a typical heavily doped semiconductor behavior.[38] S was negative for all the samples, indicating that the majority charge carrier is electrons. Owing to the slight increase in the n_H, both the ρ values and the absolute S values generally decreased with increase in the In content.

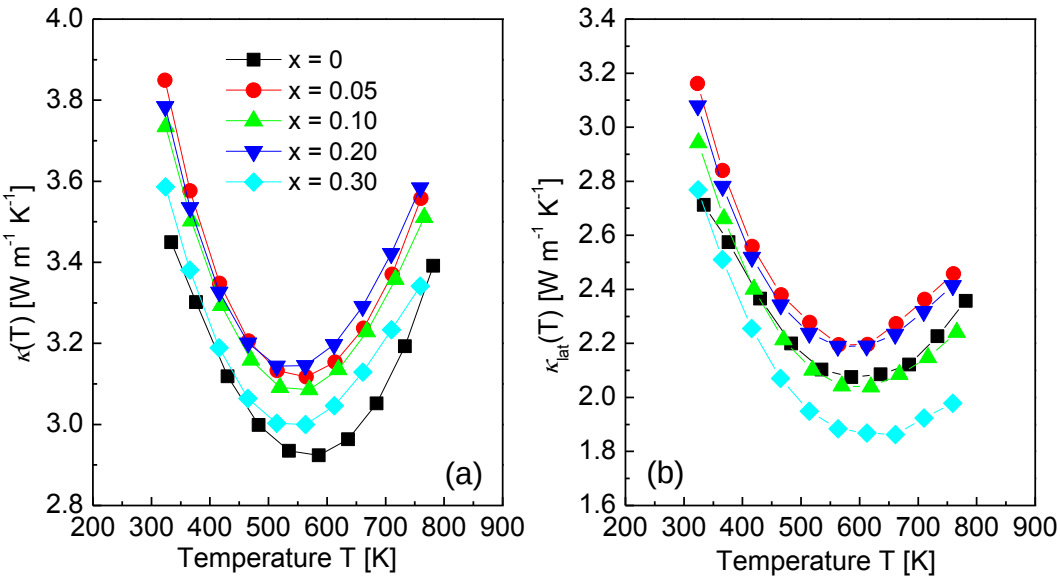

Figure 4.8 Temperature dependence of (a) thermal conductivity κ, and (b) lattice thermal conductivity κ_{lat}, for $In_xGa_{0.02}Tl_{0.20}Co_4Sb_{12}$ ($0 \le x \le 0.30$) polycrystalline samples.

As shown in Figure 4.8(a), κ decreased with increasing temperature up to around 550 K and then increased. This temperature dependence can be attributed to the bipolar conduction in semiconductors. All samples showed relatively low κ values, and the $Ga_{0.02}Tl_{0.20}Co_4Sb_{12}$ sample showed the lowest value in the whole temperature range. The κ_{lat} was obtained by subtraction of $\kappa_{el} = L\sigma T$ (where L is the Lorenz number = 2.45×10^{-8} $W\Omega K^{-2}$) from the measured κ, i.e., $\kappa_{lat} = \kappa - L\sigma T$. As shown in Figure 4.8(b), the $In_{0.30}Ga_{0.02}Tl_{0.20}Co_4Sb_{12}$ sample showed the lowest κ_{lat} values. The similar content in the filled Tl and In and the impurity phases composed mainly of In would scatter phonons efficiently, leading to the lowest κ_{lat} compared to other samples. As mentioned in chapter III, the nanoparticles with sizes smaller than 85 nm would effectively scatter heat carrying phonons. However, it is difficult to evaluate the nanoparticle effect on κ_{lat} quantitatively.

The temperature dependence of ZT is shown in Figure 4.9. The ZT increased with increasing temperature. All of the samples showed the relatively high ZT values.

The maximum *ZT* value was 0.72 at 773 K obtained for the $In_{0.30}Ga_{0.02}Tl_{0.20}Co_4Sb_{12}$ sample.

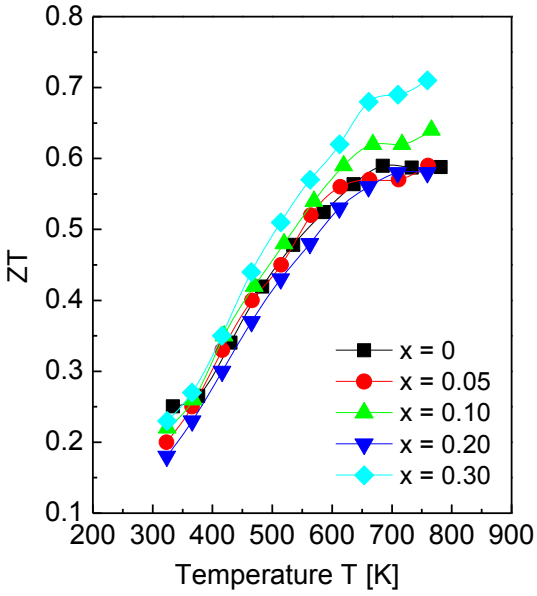

Figure 4.9 Temperature dependence of the dimensionless figure of merit *ZT* for $In_xGa_{0.02}Tl_{0.20}Co_4Sb_{12}$ ($0 \le x \le 0.30$) polycrystalline samples.

4.4 Summary

In the present study, polycrystalline samples of group 13 elements (Ga, In, and Tl) triple filled $CoSb_3$ in the compositions of $In_xGa_{0.02}Tl_{0.2}Co_4Sb_{12}$ ($0 \le x \le 0.30$) were prepared and the TE properties were investigated from room temperature to 773 K. All of the samples had a few impurity phases in addition to the skutterudite matrix phase. With increasing the amount of In, the In content increased in the skutterudite phase while the Tl content decreased. Based on the analyses of both lattice parameters and the carrier concentration, the valence state of In in the $CoSb_3$ structure would be close to +1, not +3. All of the samples exhibited negative *S* values. Owing to the slight increase in the n_H, both the ρ values and the absolute *S* values generally decreased with increase in the In content. The κ_{lat} of the samples were significantly reduced by adding the group 13 elements into $CoSb_3$. All of the samples approached relatively low κ_{lat} even they contained a few impurity phases. All of the

samples exhibited relatively high *ZT* values, the maximum *ZT* value was 0.72 at 773 K obtained for the $In_{0.30}Ga_{0.02}Tl_{0.20}Co_4Sb_{12}$ sample.

References

1) G.A. Slack: CRC Handbook of Thermoelectrics, ed. by D. M. Rowe, (CRC Press, New York, 1995), pp. 407-440.

2) G. S. Nolas, J. Sharp and H. J. Goldsmid: Thermoelectrics: Basic principles and New Materials Developments, (Springer, Berlin, 2001).

3) A. F. Ioffe: Semiconductor Thermoelements and Thermoelectric Cooling, (Infosearch Limited, London, 1957).

4) B. C. Sales, D. Mandrus and R. K. Williams: Science **272**, 1325 (1996).

5) W. Jeitschko and D. J. Brown: Acta Crystallogr. B **33**, 3401 (1977).

6) G. S. Nolas, G. A. Slack, D. T. Morelli, T. M. Tritt and A. C. Ehrlich: J. Appl. Phys. **79**, 4002-4008 (1996).

7) D. T. Morelli and G. P. Meisner: J. Appl. Phys. **77**, 3777-3781 (1995).

8) J. J. Zhang, B. Xu, L. M. Wang, D. L. Yu, Z. Y. Liu, J. L. He and Y. J. Tian: Appl. Phys. Lett. **98**, 072109 (2011).

9) Y. Z. Pei, J. Yang, L. D. Chen, W. Zhang, J. R. Salvador and J. H. Yang: Appl. Phys. Lett. **95**, 042101 (2009).

10) Y. Z. Pei, L. D. Chen, W. Zhang, X. Shi, S. Q. Bai, X. Y. Zhao, Z. G. Mei and X. Y. Li: Appl. Phys. Lett. **89**, 221107 (2006).

11) M. Puyet, B. Lenoir, A. Dauscher, M. Dehmas, C. Stiewe and E. Muller: J. Appl. Phys. **95**, 4852 (2004).

12) X. Y. Zhao, X. Shi, L. D. Chen, W. Q. Zhang, W. B. Zhang and Y. Z. Pei: J. Appl. Phys. **99**, 053711 (2006).

13) L. D. Chen, T. Kawahara, X. F. Tang, T. Goto, T. Hirai, J. S. Dyck, W. Chen and C. Uher: J. Appl. Phys. **90**, 1864 (2001).

14) G. S. Nolas, J. L. Cohn and G. A. Slack: Phys. Rev. B **58**, 164 (1998).

15) D. T. Morelli, G. P. Meisner, B. X. Chen, S. Q. Hu and C. Uher: Phys. Rev. B **56**, 7376 (1997).

16) J. Yang, Q. Hao, H. Wang, Y. C. Lan, Q. Y. He, A. Minnich, D. Z. Wang, J. A. Harriman, V. M. Varki, M. S. Dresselhaus, G. Chen and Z. F. Ren: Phys. Rev. B **80**, 115329 (2009).

17) G. A. Lamberton, Jr., S. Bhattacharya, R. T. Littleton IV, M. A. Kaeser, R. H.

Tedstrom and T. M. Tritt: Appl. Phys. Lett. **80**, 598 (2002).
18) V. L. Kuznetsov, L. A. Kuznetsova and D. M. Rowe: J. Phys.: Condesns. Matter **15**, 5035 (2003).
19) Y. P. Jiang, X. P. Jia, T. C. Su, N. Dong, F. R. Yu, Y. J. Tian, W. Guo, H. W. Xu, L. Deng and H. A. Ma: J. Alloy. Compd. **493**, 535 (2009).
20) T. He, J. Chen, D. Rosenfeld and M. A. Subramanian: Chem. Mater. **18**, (2006) 759.
21) R. C. Mallik, C. Stiewe, G. Karpinski, R. Hassdorf and E. Muller: J. Electron. Mater. **38**, 1337 (2009).
22) B. C. Sales, B. C. Chakoumakos and D. Mandrus: Phys. Rev. B **61**, 2475 (2000).
23) Y. Qiu, L. Xi, X. Shi, P. Qiu, W. Zhang, L. Chen, J. R. Salvador, J. Y. Cho, J. Yang, Y. Chien, S. Chen, Y. Tang, and G. Snyder: Adv. Funct. Mater. **23**, 3194-3203 (2013).
24) A. Harnwunggmoung, K. Kurosaki, T. Plirdpring, T. Sugahara, Y. Ohishi, H. Muta and S. Yamanaka: J. Appl. Phys. **110**, 013521 (2011).
25) G. H. Li, K. Kurosaki, Y. Ohishi, H. Muta and S. Yamanaka: J. Electron. Mater. **42**, 1463 (2012).
26) A. Harnwunggmoung, K. Kurosaki, H. Muta and S. Yamanaka: Appl. Phys. Lett. **96**, 202107 (2010).
27) A. Harnwunggmoung, K. Kurosaki, A. Kosuga, M. Ishimaru, T. Plirdpring, R. Yimnirun, J. Jutimoosik, S. Rujirawat, Y. Ohishi, H. Muta and S. Yamanaka：J. Appl. Phys. **112**, 043509 (2012).
28) S. Ballikaya, G. Wang, K. Sun and C. Uher: J. Electron. Mater. **40**, 570 (2011).
29) G. Rogl, Z. Aabdin, E. Schafler, J. Horky, D. Setman, M. Zehetbauer, M. Kriegisch, O. Eibl, A. Grytsiv, E. Bauer, M. Reinecker, W. Schranz and P. Rogl: J. Alloys. Compd. **537**, 183 (2012).
30) S. Ballikaya, N. Uzar, S. Yildirim, J. R. Salvador and C. Uher: J. Solid State Chem. **193**, 31 (2012).
31) S. Ballikaya, G. Wang, K. Sun and C. Uher: J. Electron. Mater. **40**, 570 (2011).
32) H. Li, X. F. Tang, Q. J. Zhang and C. Uher: Appl. Phys. Lett. **94**, 102114 (2009).
33) L. Xi, J. Yang, C. F. Lu, Z. G. Mei, W. Q. Zhang and L. D. Chen: Chem. Mater. **22**, 2384 (2010).

34) L. Pauling: The Nature of the Chemical Bond, (Cornell University Press, New York, 1960).
35) Y. Tang, Y. Qiu, L. Xi, X. Shi, W. Zhang, L. Chen, S. Tseng, S. Chen and G. Snyder: The 32nd Int. Conf. On Thermoelectrics, (Kobe, Japan, 2013) B1-04.
36) R. C. Mallik, J. Y. Jung, S. C. Ur and I. H. Kim: Metals Mater. Int. **14**, 223 (2008).
37) W. Y. Zhao, C. L. Dong, P. Wei, W. Guan, L. S. Liu, P. C. Zhai, X. F. Tang and Q. J. Zhang: J. Appl. Phys. **102**, 113708 (2007).
38) R. C. Mallik, C. Stiewe, G. Karpinski, R. Hassdorf and E. Muller: Proc. 6th European Conf. on Thermoelectrics, (Paris, France, 2008) P1-25-1-5.

CHAPTER V

Effect of Tl and K Double-Filling on Thermoelectric Properties of $CoSb_3$

5.1 Introduction

Thermoelectric (TE) materials can be used for direct energy conversion from waste heat into electrical power, and have the merit of no moving parts and high reliability. The efficiency of the energy conversion of TE materials is governed by the dimensionless figure of merit, $ZT = S^2T/\rho/\kappa$. In this equation, S is the Seebeck coefficient, T is the absolute temperature, ρ is the electrical resistivity, and κ is the total thermal conductivity ($\kappa = \kappa_{lat} + \kappa_{el}$, where κ_{lat} and κ_{el} are the lattice and electronic contributions, respectively).[1)] Owing to the ZT value directly reflects the efficiency of the energy conversion, the development of high-ZT materials has a significant meaning for more effective energy savings by recycling the waste heat. To achieve high ZT, a large S, low ρ, and low κ are required, however, S, ρ, and κ_{el} are strongly interrelated with each other in materials, so reduction of κ_{lat} is required to maximize ZT.[2, 3)]

With the significant reduction of κ_{lat} due to the strong “rattling” phonon scattering effect by filler atoms, filled skutterudites have been a focus of research as typical “phonon-glass electron-crystal” materials proposed by Slack for their promising thermoelectric performance in practical application.[1)] The alkaline-earth (AE) or rare-earth (RE) metals filled skutterudites with ZT above unity value have been reported widely.[4-9)] In comparison, other group elements-filled skutterudites were rarely reported. Among them, both of K and Tl single-element-filled skutterudites showed ZT around 1.[10,11)] Recently, the vibrational frequencies of the filler atoms in $CoSb_3$ have been calculated by density functional theory and were found to be significantly different for different chemical groups of the periodic table.[12)]

It was suggested that only the lattice phonons with frequencies near the vibrational frequency of fillers can be strongly scattered via phonon resonant scattering.[13] Therefore, introducing two different chemical groups into the cages of $CoSb_3$ could introduce two distinctive filler vibrational frequency for a broader range lattice phonon scattering, leading to a further κ_{lat} reduction.[13] In the present study, we selected one of the lightest elements K and one of the heavy element Tl as a combination for co-filling, i.e. the vibrational frequencies between them should be large. And consider both of them are very effective for reduce the lattice thermal conductivity as single-filling elements as reported literature, the more significant reduction of lattice thermal conductivity can be expected by Tl and K co-filling.

Consider K is drastically evaporate at high temperature, however according to the previous literature,[10] 30% addition of K can make sure around 10% can be actually filled into the cages. Although, Tl's filling limit is around 20%, consider the filling fraction limit of K was determined as high as 45%, therefore, more than 20% of Tl can be expected to be filled into Co_4Sb_{12} completely. Therefore, the sample compositions were determined as $Tl_xK_{0.3}Co_4Sb_{12}$ ($0.1 \leq x \leq 0.30$).

5.2 Experimental

The Tl and K double-filled skutterudites: $Tl_xK_{0.3}Co_4Sb_{12}$ ($0.1 \leq x \leq 0.30$) were synthesized by a combination method of traditional melting and long-term high-temperature annealing. The high-purity elements Tl (99.9%), K (99%), Co (99.99%) and Sb (99.999%) were combined in their stoichiometric ratios and placed in a carbon crucible, and then loaded into a silicon tube in a glove-box under an Ar flow atmosphere. The silica tubes were sealed under vacuum. The sealed silica tubes were heated slowly up to 1323 K and then quenched to room temperature. And then, annealed at 873 K for one week. The obtained ingots were crushed into powders, followed by spark plasma sintering at 923 K under a pressure of 50 MPa for 15 minutes in an Ar flow atmosphere.

Structural characterization was conducted using X-ray diffraction (XRD) analysis in air at room temperature with Cu Kα radiation. The microstructure and chemical composition of the samples were investigated by field emission scanning electron microscopy (FE-SEM; JEOL JSM-6500F) with energy dispersive X-ray (EDX) analysis in vacuum at room temperature. S and ρ were measured using a commercially available apparatus (ULVAC, ZEM-1) in a He atmosphere. Thermal diffusivity (α) was measured by the laser flash method in a vacuum using a commercially-available thermal constant analyzer (ULVAC TC-7000). κ was evaluated via the standard equation of $\kappa = \alpha C_p d$, where C_p and d are heat capacity and density, respectively. C_p was estimated using the Dulong-Petit model, i.e., $C_p = 3nR$, where n is the number of atoms per formula unit and R is the gas constant. All TE properties were measured from room temperature to 773 K.

Hall coefficient (R_H) was measured at room temperature by the van der Pauw method under vacuum with an applied magnetic field of 0.5 T. The Hall carrier concentration (n_H) and Hall mobility (μ_H) were calculated from R_H assuming a single band model and a Hall factor of 1, i.e., $n_H = 1/(eR_H)$ and $\mu_H = R_H/\rho$, where e is the elementary electric charge. The density of bulk samples was calculated on the basis of the samples' weight and dimensions.

5.3 Results and Discussion

The powder XRD patterns of the polycrystalline samples of $Tl_xK_{0.3}Co_4Sb_{12}$ ($0.1 \le x \le 0.30$) are shown in Figure 5.1. From the results, it can be found that all samples were single phase and that all the peaks in the XRD patterns were identified as peaks derived from the skutterudite phase. And the lattice parameters calculated from the XRD patterns of $Tl_xK_{0.3}Co_4Sb_{12}$ ($0.1 \le x \le 0.30$) are plotted in Figure 5.2. The lattice parameters were increased obviously with increasing Tl contents.

Figure 5.3 show SEM and EDX mapping images for sample of $Tl_{0.3}K_{0.3}Co_4Sb_{12}$. The surface was homogeneous with no significant trace of impurity phases by EDX analysis. The matrix chemical compositions of samples were

determined by EDX analysis, and the results were summarized in Table 5.1. As shown in Table 5.1, all of the Tl was successfully filled into the cages in all of the samples even 30% Tl amounts exceed the filling fraction limit. It indicates that K which has high filling fraction limits around 45% can driving up Tl's solubility in $CoSb_3$ base skutterudites. And, the main reason for the significant difference between the nominal and measured value in K contents is the considerable volatilization losses of K during the synthesis. Due to, the high amounts of filler atoms filled into the matrix, the carrier concentration as high as 4.3 X 10^{20} cm^{-3} was obtained for $Tl_{0.3}K_{0.3}Co_4Sb_{12}$. In addition, all the samples used for hall coefficient measurement were approached to their theoretical density.

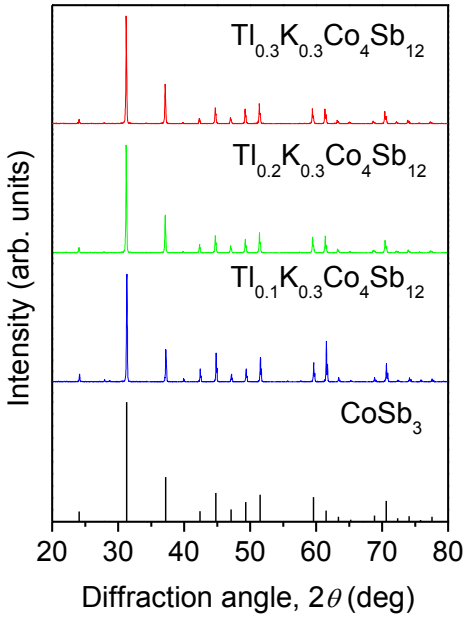

Figure 5.1 Powder XRD patterns of polycrystalline samples of $Tl_xK_{0.3}Co_4Sb_{12}$ (x = 0.1~0.3).

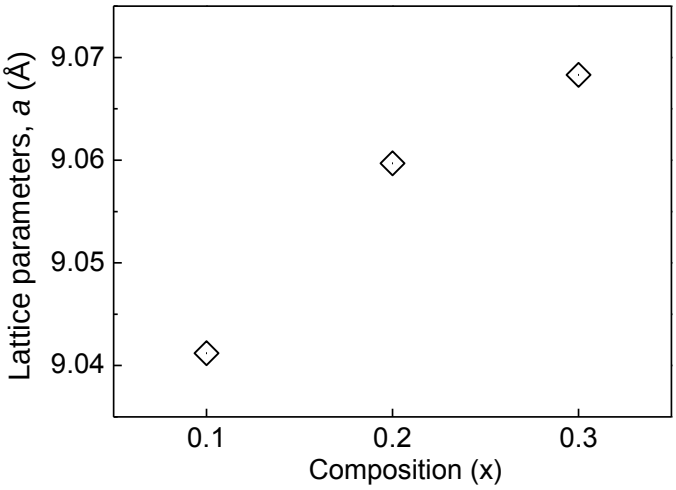

Figure 5.2 Lattice parameters of polycrystalline samples of $Tl_xK_{0.3}Co_4Sb_{12}$ (x = 0.1~0.3).

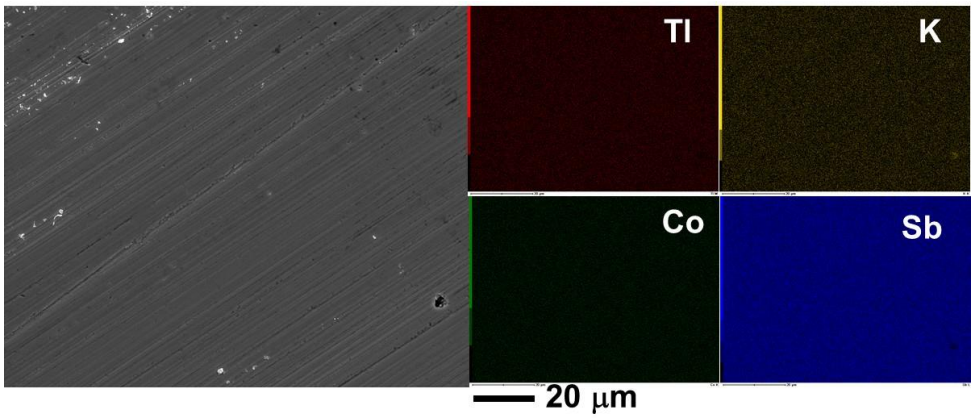

Figure 5.3 FE-SEM micrographic and EDX elemental maps for $Tl_{0.3}K_{0.3}Co_4Sb_{12}$ sample.

Table 5.1 Compositions and charge-transport Properties of Tl and K double-filled skutterudites at room temperature

Normal composition	EDX composition	R_H ($10^{-2}cm^3C^{-1}$)	n_H (10^{20} cm^{-3})	μ_H ($cm^{-2}V^{-1}s^{-1}$)
$Tl_{0.1}K_{0.3}Co_4Sb_{12}$	$Tl_{0.1}K_{0.15}Co_{3.8}Sb_{12.4}$	2.4	1.5	52.2
$Tl_{0.2}K_{0.3}Co_4Sb_{12}$	$Tl_{0.2}K_{0.2}Co_{3.8}Sb_{12.3}$	2	3	42.1
$Tl_{0.3}K_{0.3}Co_4Sb_{12}$	$Tl_{0.3}K_{0.2}Co_{3.8}Sb_{12.3}$	1.5	4.3	38.5

The temperature dependence of TE properties are shown in Figure 5.4. Figure 5.4 (a) shows an increase in ρ with temperature, exhibits a typical heavily doped semiconductor behavior as reported by Mallik et al.[14] And ρ decreased with Tl contents, it can be considered that the n_H increased with increasing Tl contents in the matrix, although the carrier mobility was slightly decreased. Figure 5.4 (b) shows that the *S* decreased with increasing Tl contents. Since the *S* and n_H is inversely proportional, this phenomenon also can be explained by n_H increased with Tl addition. In the cases of x = 0.2 and 0.3, the *S* increased with temperature, however, *S* increased with temperature up to 600 K and then decreased for x = 0.1.

Figure 5.4 (c), (d), and (e) show the temperature dependence of κ, $\kappa_{lat,}$ and κ_{ele} respectively. As shown in Figure 5.4 (c) and (d), x = 0.20 sample showed the lowest κ, however, the x = 0.30 sample shows the lowest κ_{lat} in the entire temperature range. It can be exlained by the κ_{ele} of x = 30 is much higher than that of x = 20 in the entire temperature range due to the higher carrier concentration as shown in Table 5.1. In addition, the bipolar effect in the x = 0.1 sample is much obvious than that of x = 0.2 and 0.3. This can be considered that, high carrier concentration in x = 0.2 and 0.3 samples effectively depressed the bipolar effect at high temperature resulted in a lattice thermal conductivity as low as 0.9 $Wm^{-1}K^{-1}$. It indicates that Tl and K co-filling is an effective way to scatter the thermal carrying phonons. The bipolar effect also can be observed from the temperature dependence of *S* as shown in Figure 5.3 (b). Figure 5.3 (f) shows the temperature dependence of *ZT*. Duo to, the enhanced electrical properties, and the significantly reduced thermal conductivity, the maximum *ZT* of 1 was obtained at 773 K for $Tl_{0.2}K_{0.3}Co_4Sb_{12}$ and $Tl_{0.3}K_{0.3}Co_4Sb_{12}$ in the nominal compositions.

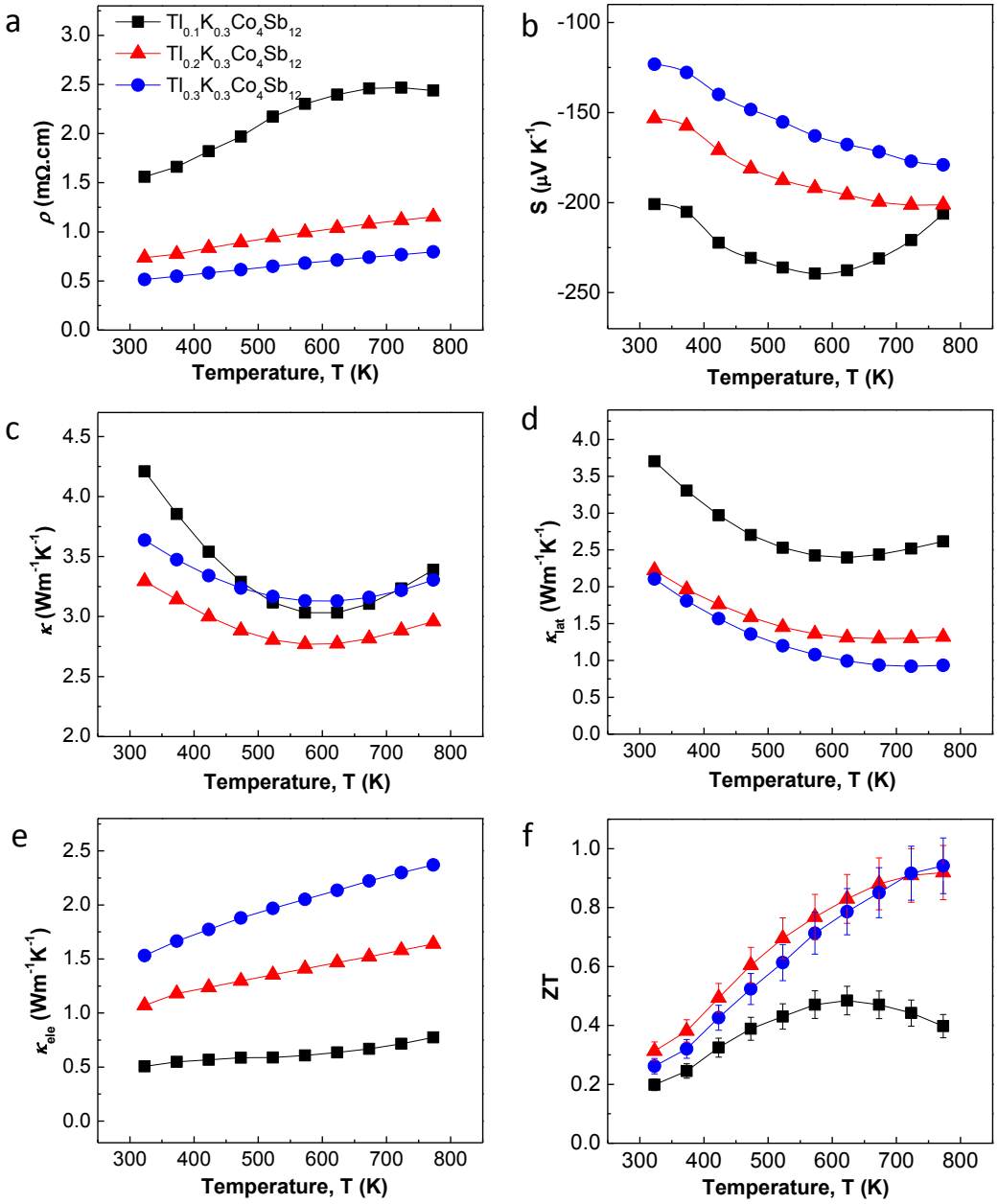

Figure 5.4 The TE properties of polycrystalline samples of $Tl_xK_{0.3}Co_4Sb_{12}$ (x = 0.1~0.3).

5.4 Summary

In the present study, Tl and K co-filled skutterudites, $Tl_xK_{0.3}Co_4Sb_{12}$ ($0.1 \leq x \leq 0.30$) was prepared and their TE properties were investigated. All of the samples

showed single phase. Owing to the high filling amounts, the electrical properties were obviously enhanced. At the same time, a very low lattice thermal conductivity was obtained in the entire temperature range for x = 0.3. It indicates that Tl and K co-filling is an effective way for phonon scattering. The maximum ZT of around unity was obtained at 773 K for $Tl_{0.3}K_{0.3}Co_4Sb_{12}$ and $Tl_{0.2}K_{0.3}Co_4Sb_{12}$ in the nominal compositions.

References

1) G.A. Slack: CRC Handbook of Thermoelectrics, ed. by D. M. Rowe, (CRC Press, New York, 1995), pp. 407-440.
2) G. S. Nolas, J. Sharp and H. J. Goldsmid: Thermoelectrics: Basic principles and New Materials Developments, (Springer, Berlin, 2001).
3) A. F. Ioffe: Semiconductor Thermoelements and Thermoelectric Cooling, (Infosearch Limited, London, 1957).
4) L. D. Chen, T. Kawahara, X. F. Tang, T. Goto, T. Hirai, J. S. Dyck, W. Chen, and C. Uher, J. Appl. Phys. 90, 1864（2001).
5) X. Y. Zhao, X. Shi, L. D. Chen, W. Q. Zhang, W. B. Zhang, and Y. Z. Pei, J. Appl. Phys. 99, 053711 (2006).
6) M. Puyet, B. Lenoir, A. Dauscher, M. Dehmas, C.Stiewe, and E. Muller, J. Appl. Phys. 95, 4852 (2004).
7) G. A. Lamberton, Jr, S. Bhattacharya, R. T. Littleton IV, M. A. Kaeser, R. H. Tedstrom, T. M. Tritt, J. Yang, and G. S. Nolas, Appl. Phys. Lett. 80, 598 (2002).
8) D. T. Morelli, G. P. Meisner, B. Chen, S. Hu, and C. Uher, Phys. Rev. B 56, 7376 (1997).
9) G. S. Nolas, M. Kaeser, R. T. Littleton, and T. M. Tritt, Appl. Phys. Lett. 77, 1855 (2000).
10) Y. Z. Pei, L. D. Chen, W. Zhang, X. Shi, S. Q. Bai, X. Y. Zhao, Z. G. Mei, and X. Y. Li, Appl. Phys. Lett. 89, 221107 (2006).
11) A. Harnwunggmoung, K. Kurosaki, H. Muta, and S. Yamanaka, Appl. Phys. Lett. 96, 202107 (2010).
12) J. H. Yang, W. Zhang, S. Q. Bai, Z. Mei, L. D. Chen, Appl. Phys. Lett. 90, 192111 (2007).
13) X. Shi, H. Kong, C. P. Li, C. Uher, J. Yang, J. R. Salvador, H. Wang, L. Chen, W. Zhang, Appl. Phys. Lett. 92, 182101 (2008).
14) R. C. Mallik, C. Stiewe, G. Karpinski, R. Hassdorf, and E. Muller, Proceedings of the 6th European Conference on Thermoelectrics (ETC.-2008), Paris, France, P1-25-1-5 (2008).

CHAPTER VI

High Temperature Thermoelectric Properties of Half-Heusler Compound PtYSb

6.1 Introduction

Thermoelectric (TE) materials can be used for energy conversion from heat into electrical power. The efficiency of TE materials for energy conversion is determined by the dimensionless figure of merit, $ZT = S^2T\rho^{-1}\kappa^{-1}$, where S is the Seebeck coefficient, T is the absolute temperature, ρ is the electrical resistivity, and κ is the total thermal conductivity ($\kappa = \kappa_{lat} + \kappa_{el}$, where κ_{lat} and κ_{el} are the lattice and electronic contributions, respectively).[1,2] The ZT value directly reflects the efficiency for energy conversion; therefore, the development of high-ZT materials is the main goal in this research area. According to the ZT equation, large S, low ρ, and low κ, which are interrelated transport properties, are required to maximize ZT.[3]

Half-Heusler compounds have received much attention in recent years as advanced TE materials, due to their tunable band gap size, which has resulted in multifarious physical properties. The TE properties of various half-Heusler compounds such as *M*NiSn,[4-11] *M*CoSb,[12,13] HfPtSn,[14] and *Ln*PdSb,[15] where *M* = Ti, Zr, Hf and *Ln* = lanthanide elements, with valence electron concentrations (VEC) of 18, have been experimentally confirmed as compounds that exhibit ideal transport properties as TE materials due to their narrow band gap or pseudo-gap at the Fermi level. Shen et al. achieved ZT = 0.7 at 800 K for partially Pd-substituted ZrNiSn.[6] Sakurada and Shutoh reported the Sb-doped (Ti,Zr,Hf)NiSn with ZT = 1.5 at 700 K, due to the large S and a very low κ,[8] which is one of the highest ZT values in bulk TE materials within the intermediate temperature range.

It has been demonstrated that several half-Heusler compounds containing noble metals such as Pd and Pt exhibit excellent TE properties. Oestreich et al. have studied the TE properties of $ScM^{VIII}Sb$ and $YM^{VIII}Sb$ (M^{VIII} = Ni, Pd, Pt), and expected that PtYSb would be a promising TE candidate material, based on the large power factor $S^2\rho^{-1}$, and low κ.[16] Ouardi et al. reported that PtYSb has a large mobility of 300 $cm^2\ V^{-1}\ s^{-1}$ at 350 K, which resulted in a relatively high *ZT* value of 0.2 at 350 K.[17,18]

The relatively high *ZT* values for PtYSb reported to date have motivated us to investigate this compound further. The previous work has reported the TE properties of PtYSb only in the low-temperature range, and no high-temperature data have yet been reported. Therefore, in the present study, polycrystalline bulk samples of PtYSb were prepared and their high-temperature TE properties were examined.

6. 2 Experimental

Polycrystalline samples of PtYSb were prepared from a stoichiometric ratio of Pt (99.9%) wire, Y (99%) chunks, and Sb (99.9%) chunks. The staring materials were weighed and mixed in a glove box under a N_2-flow atmosphere, and then placed into silica tubes. The silica tubes were sealed and slowly heated up to 1323 K and held for 1 week, then annealed at 1123 K for 2 weeks. The resultant ingots were crushed into fine powders, followed by spark plasma sintering (SPS) in a graphite die at 1073 K under a pressure of 60 MPa for 20 min under an Ar-flow atmosphere.

Structural characterization was conducted using powder X-ray diffraction (XRD) analysis in air at room temperature using Cu $K\alpha$ radiation. The microstructure and elemental distribution of the sample surface were investigated using field emission scanning electron microscopy (FE-SEM; Jeol, JSM-6500F) and energy dispersive X-ray (EDX) spectroscopy under vacuum at room temperature. Cylindrical samples (10 mm diameter, 15 mm height) were used for *S*, ρ, and sound velocity measurements and disc-shaped samples (10 mm diameter, 1 mm thick) were used for thermal diffusivity (α) and Hall coefficient (R_H) measurements. *S* and ρ were

measured using a commercially available apparatus (Ulvac, ZEM-1) in a He atmosphere. α was measured by the laser flash method under vacuum using a commercially available thermal constant analyzer (Ulvac TC-7000). κ was evaluated via the standard equation of $\kappa = \alpha C_p d$, where C_p and d are the heat capacity and density, respectively. C_p was estimated using the Dulong-Petit model, i.e., $C_p = 3nR$, where n is the number of atoms per formula unit and R is the gas constant.

All of the TE properties were measured from room temperature to 973 K. R_H was measured at room temperature by the van der Pauw's method under vacuum with an applied magnetic field of 0.5 T. The Hall carrier concentration (n_H) and Hall mobility (μ_H) were calculated from R_H assuming a single band model and a Hall factor of 1, i.e. $n_H = 1/eR_H$ and $\mu_H = R_H/\rho$, where e is the elementary electric charge. The density of bulk samples was calculated on the basis of the measured sample weight and dimensions. Longitudinal and shear sound velocities were measured using the cylindrical samples with the ultrasonic pulse echo method to calculate the Debye temperature (θ_D).

6. 3 Results and Discussion

Powder XRD patterns of the polycrystalline PtYSb samples are shown in Figure 6.1, together with the literature data for reference.[19] Almost all the peaks in the XRD patterns were consistent with that reported for PtYSb.[19] Several negligible peaks corresponding to yttrium oxide (Y_2O_3) and Pt_3Y were observed as impurity phases.

As summarized in Table 6.1, the lattice parameter was determined to be 0.6538 nm for the prepared sample, which is in good agreement with the literature values of 0.6532 and 0.6527 nm.[16,18]

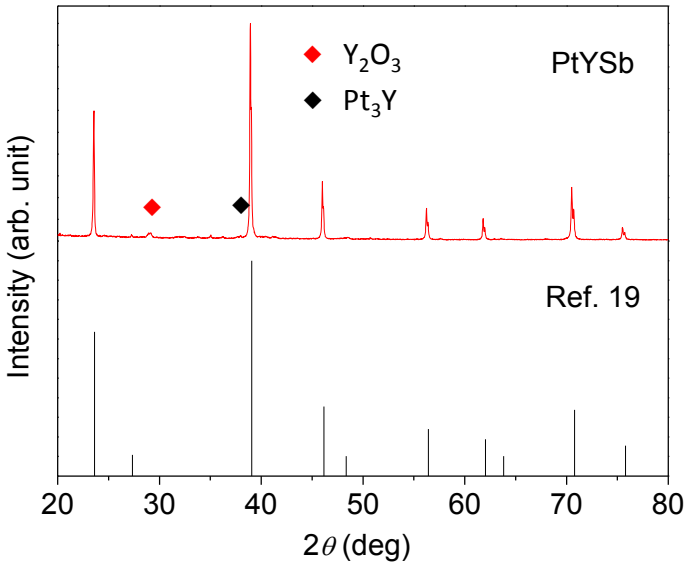

Figure 6.1 Powder XRD patterns of the PtYSb sample prepared in this study and that reported in Ref. 19.

Table 6.1 Lattice parameters *a*, density *d*, percentage theoretical density (% T.D.), longitudinal sound velocity V_L (m/s), shear sound velocity V_S (m/s), Hall coefficient RH (300 K), Hall carrier concentration n_H (300 K), Hall mobility μ_H (300 K), and Debye temperature θ_D, for the polycrystalline PtYSb sample.

Sample	*a* (nm)	*d* (g cm^{-3})	% T.D.	V_L (m/s)	V_S (m/s)	θ_D (K)
	0.6538	8.92	92.4	4408.91	2512.11	283
PtYSb	R_H (cm^3/C)	n_H (10^{19}cm^{-3})	μ_H (cm^{2}V^{-1}s^{-1})			
	0.346	1.81	164			

An SEM micrograph and EDX elemental maps of the SPS PtYSb sample are shown in Figure 6.2. The impurity phases were clearly evident in the SEM image. In addition, the chemical composition was obtained through EDX point analysis as shown in Table 6.2.

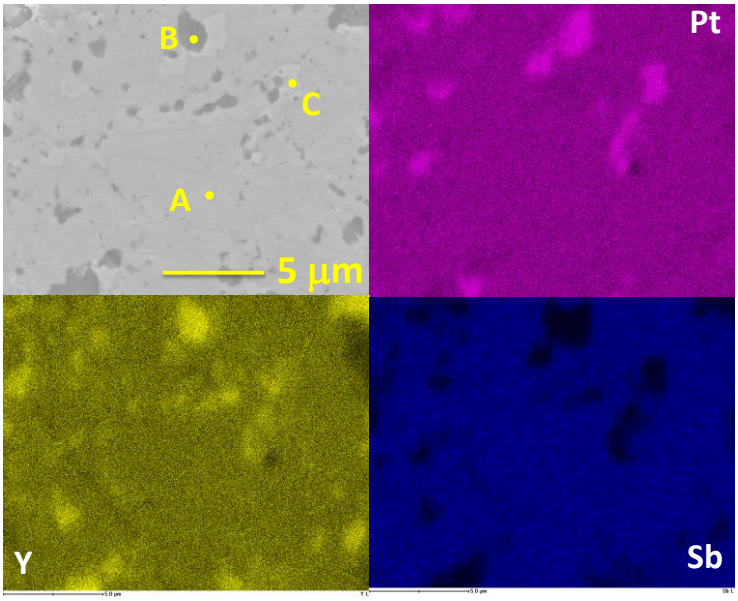

Figure 6.2 FE-SEM micrograph and EDX elemental maps for the PtYSb sample.

Table 6.2 Chemical compositions of points A, B and C (at. %) determined by EDX point analysis

	A	B	C
Pt	36.12%	3.18%	73.24%
Y	31.07%	42.52%	19.86%
Sb	32.81%	0.53%	4.10%
O	0%	53.77%	2.80%

The points of A, B, and C were chosen within main matrix phase, Pt rich phase, and Y rich phase respectively. From the result of EDX point analysis, the actual chemical composition of main matrix was determined to $PtY_{0.86}Sb_{0.91}$, and as for Pt rich phase and Y rich phase, combine together with XRD patterns the impurity phases were determined to Pt_3Y and Y_2O_3 respectively. The reason for Sb lost is that is that Sb is easily vaporize during melting at high temperature condition. As mentioned before, the actual chemical composition of main matrix is $PtY_{0.86}Sb_{0.91}$, which leads to the formation of vacancies in the phase. Therefore, it is important to

consider the effect of the vacancies in the half-heusler phase is helpful for reduction of the lattice thermal conductivity by phonon scattering, while the vacancies also scatter carriers which results in the reduction of the carrier mobility. The reduced carrier mobility also lead to higher electrical resistivity.

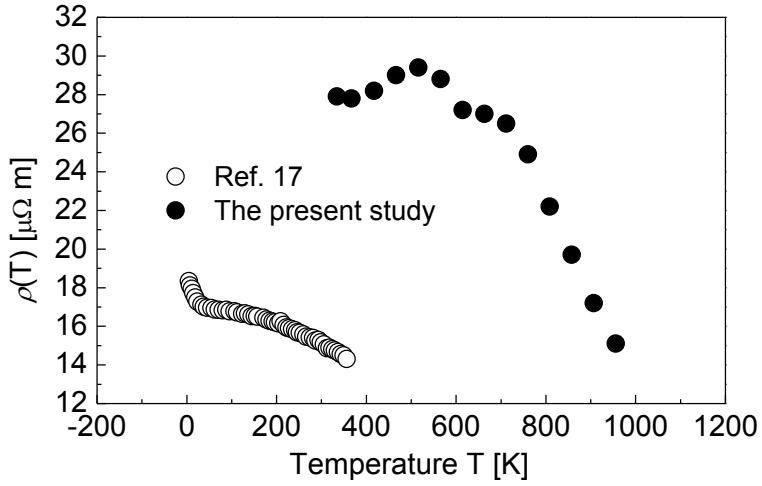

Figure 6.3 Temperature dependency of the electrical resistivity, ρ for the PtYSb sample, together with that reported in Ref. 17.

The temperature dependency of the electrical resistivity ρ for the PtYSb sample are shown in Figures 6.3, in addition to the low-temperature data reported in Ref. 17 for comparison. Figure 6.3(a) shows an increase in ρ with temperature up to around 500 K, followed by a decrease. The metal like behavior at low temperature range probably due to VEC affected by element lost. The ρ values are almost two times higher than the literature data.[17] Table 6.1 shows that μ_H for the sample was 164 $cm^2\ V^{-1}\ s^{-1}$ at room temperature, which was almost half that reported in Ref. 17 (300 $cm^2\ V^{-1}\ s^{-1}$). This is probably due to charge carrier scattering at the grain boundaries and vacancies generated by element lost, in addition to impurities, cracks, and pores present in the polycrystalline sample. The relative density of the sample was 92.4% of the theoretical density.

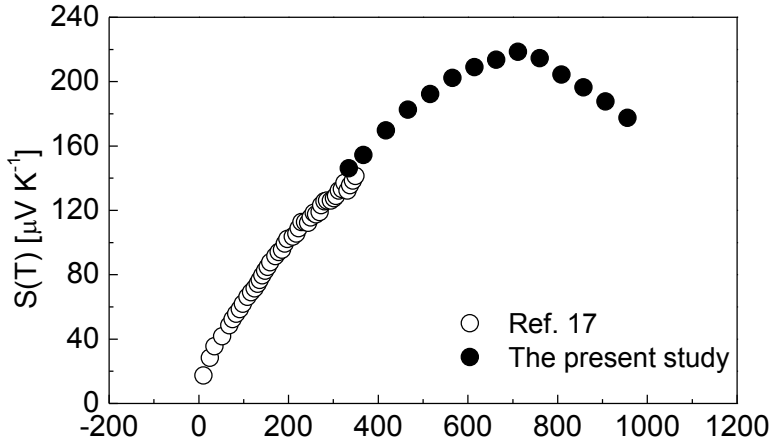

Figure 6.4 Temperature dependency of the Seebeck coefficient, *S* for the PtYSb sample, together with that reported in Ref. 17.

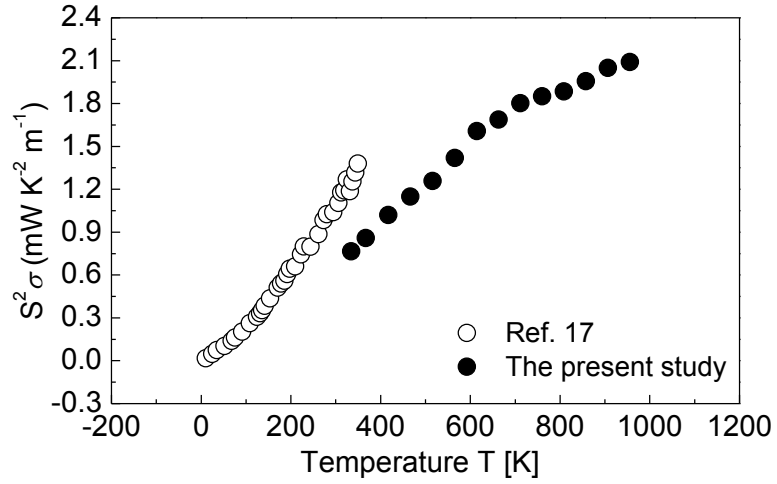

Figure 6.5 Temperature dependency of the power factor, $S^2\sigma$ for the PtYSb sample, together with that reported in Ref. 17.

Figure 6.4 shows that the *S* values were positive over the entire temperature range, which indicates that holes were the majority charge carrier. A relatively high *S* value of 146 μV K^{-1} was obtained at 350 K, which was consistent with the literature data (142 μV K^{-1}).[17] Table 6.1 shows that the n_H for the sample was 1.81×10^{19} cm^{-3}

at room temperature. S increased with the temperature up to around 700 K and then decreased.

The temperature dependence of the power factor $S^2\rho^{-1}$ is shown in Figure 6.5; the value of $S^2\rho^{-1}$ obtained at around room temperature was clearly lower than that reported in Ref. 17, due to the lower ρ compared with Ref. 17. $S^2\rho^{-1}$ increased with the temperature and reached a maximum of 2.1×10^{-3} W m^{-1} K^{-2} at 973 K.

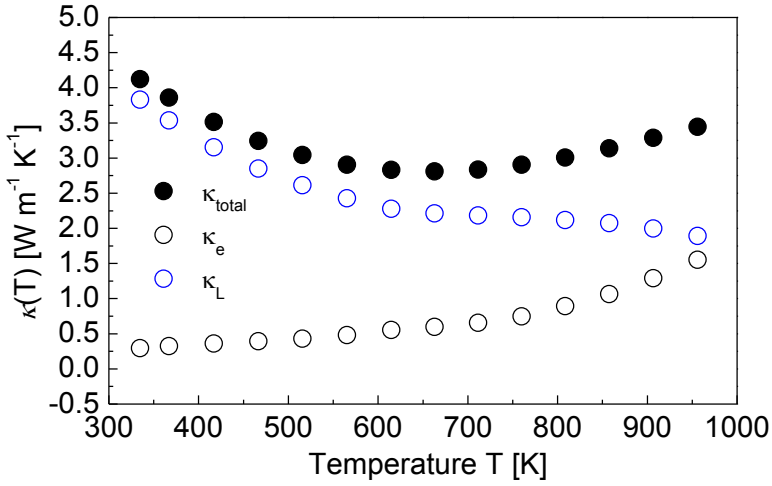

Figure 6.6 Temperature dependency of the total thermal conductivity, κ, lattice thermal conductivity, κ_{lat}, and the electrical thermal conductivity, κ_{ele} for the PtYSb sample, together with that reported in Ref. 17.

Figure 6.6 shows the temperature dependence of κ for the PtYSb sample. The κ value at room temperature was 4.2 W m^{-1} K^{-1}, which is relatively high, due to the simple cubic crystal structure and the high Debye temperature (θ_D = 283 K) for PtYSb. κ_{lat} was obtained by subtracting κ_{el} (= $LT\rho^{-1}$, where L is the Lorenz number = 2.45×10^{-8} W Ω K^{-2}) from the measured κ, i.e., $\kappa_{lat} = \kappa - LT\rho^{-1}$. The temperature dependency of κ_{lat} and κ_{el} are shown in Figure 6.4. κ_{lat} decreased almost monotonically with increasing temperature, while κ decreased with increasing temperature and then increased at around 700 K. The temperature dependence of

κ can be attributed to the increase in κ_{el} at high temperature. It has been reported that κ at room temperature for PtYSb is 2.7 W m^{-1} K^{-1},[17] which is approximately 1.5 W m^{-1} K^{-1} lower than that obtained in the present study. However, the reason for this difference is still unclear.

The temperature dependence of *ZT* for the PtYSb sample is shown in Figure 6.7, where *ZT* increased with increasing temperature. Although the *ZT* value at room temperature was lower than the literature data,[17] *ZT* increased with the temperature and reached a maximum of 0.57 at 973 K.

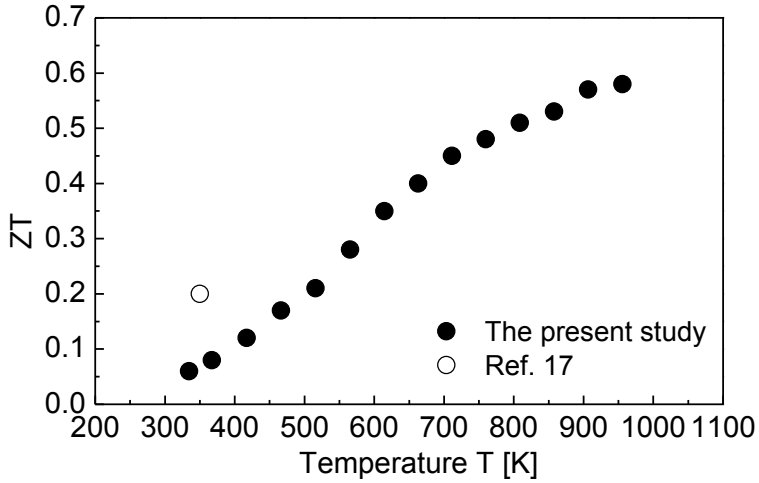

Figure 6.7 Temperature dependency of the dimensionless figure of merit, *ZT* for the PtYSb sample, together with that reported in Ref. 17.

6.4 Summary

In summary, the high-temperature TE properties of polycrystalline bulk samples of PtYSb were investigated. *S* in the given temperature range was positive for PtYSb, which indicates that holes were the majority charge carriers. Although ρ was higher than the literature data[17] at around room temperature, mainly due to grain boundary and impurity scatterings, the power factor reached a considerably high

value of 2.1×10^{-3} W m^{-1} K^{-2} at 973 K. κ decreased with increasing temperature and increased above 700 K, due to the increase of κ_{el} at high temperature. Although Y_2O_3 and Pt_3Y were present as impurity phases in the PtYSb sample and the sample density was not high (92.4%T.D.), a relatively high *ZT* of 0.57 was obtained at 973 K for the bulk sample of polycrystalline PtYSb. We expect that further enhancement in *ZT* could be achieved if samples without impurity phases and with higher density could be prepared.

References

1) D.M. Rowe (Ed.): CRC Handbook of Thermoelectrics (CRC Press, New York, 1995) p. 407-440.
2) T.M. Tritt and M.A. Subramanian: MRS Bull. **31**, 188 (2006).
3) G.J. Snyder and E.S. Toberer: Nat. Mater. **7**, 105 (2008).
4) F.G. Aliev, V.V. Kozyrkov, V.V. Moshchalkov, R.V. Scolozdra, and K. Durczewski: Z. Phys. B: Condens. Matter **80**, 353 (1990).
5) C. Uher, J. Yang, and S. Hu: Phys. Rev. B **59**, 8615 (1999).
6) Q. Shen, L. Chen, T. Goto, T. Hirai, J. Yang, G.P. Meisner, and C. Uher: Appl. Phys. Lett. **79**, 4165 (2001).
7) S. Bhattacharya and T.M. Tritt: Appl. Phys. Lett. **81**, 43 (2002).
8) S. Sakurada and N. Shutoh: Appl. Phys. Lett. **86**, 082105 (2005).
9) H. Muta, T. Kanemitsu, K. Kurosaki, and S. Yamanaka: Mater. Trans. JIM **47**, 1453 (2006).
10) S.R. Culp, S.J. Poon, N. Hickman, T.M. Tritt, and J. Blumm: Appl. Phys. Lett. **88**, 042106 (2006).
11) E. Arushanov, W. Kaefer, K. Fess, C. Kloc, K. Friemelt, and E. Bucher: Phys. Status Solidi A **177**, 511 (2000).
12) T. Sekimoto, K. Kurosaki, H. Muta, and S. Yamanaka: J. Alloys Compd. **407**, 326 (2006).
13) M. Zhou, L. Chen, C. Feng, D. Wang, and J. Li: J. Appl. Phys. **101**, 113714 (2007).
14) Y. Kimura and A. Zama: Appl. Phys. Lett. **89**, 172110 (2006).
15) T. Sekimoto, K. Kurosaki, H. Muta, and S. Yamanaka: Appl. Phys. Lett. **89**, 092108 (2006).
16) J. Oestreich, U. Probst, F. Richardt, and E. Bucher: J. Phys. Condens. Matter **15**, 635 (2003).
17) S. Ouardi, G.H. Fecher, C. Felser, J. Hamrle, K. Postava, and J. Pistora: Appl. Phys. Lett. **99**, 211904 (2011).
18) S. Ouardi, C. Shekhar, G.H. Fecher, X. Kozina, G. Stryganyuk, C. Felser, S. Ueda, and K. Kobayashi: Appl. Phys. Lett. **98**, 211901 (2011).
19) A.E. Dwight: 11th Rare Earth Res. Conf. **2**, 642 (1974).

CHAPTER VII

Summary

In the present study, the group 13 elements (Ga, In, and Tl) filled $CoSb_3$ based skutterudites compounds were prepared and their TE properties were studied in detail. Recent years, our group have focused on group 13 elements filled skutterudite compounds. Harnwunggmoung et al. have reported several papers for their TE properties. Among them, the *ZT* of Tl single-filled one approached to unity, and Tl and In double-filled one approached as high as 1.2. These results demonstrates that Tl is effective filler to reduce thermal conductivity result in an enhancement of *ZT*, although, Tl and other elements in group 13 (Ga and In) were considered that can't be filled into the cages by theoretical calculations. In filled skutterudites with high *ZT* around unity were studied by other groups, however there was a controversy for the filling fraction limit. In addition, Ga and In have widely studied as one of the co-filled fillers in skutterudites, and both of them were considered that to naturally form nano inclusions, which in composition of *X*Sb (*X* = Ga, In), on the grain boundaries result in a remarkable reduction of thermal conductivity.

Based on such research background, we focused on to determine the filling fraction limit of In in $CoSb_3$ based skutterudites firstly. According to the results of lattice parameters calculation based on XRD analysis and EDX composition analysis, we found that the filling fraction limit of In is around 8% in $CoSb_3$ based skutterudites. And also determined that In not only can be filled into the cages, but also to form InSb as impurity phase in the grain boundaries and matrix. And such finely dispersed impurity made a positive effect for reduction of thermal conductivity result in a relatively high *ZT* of 0.7 for $In_{0.35}Co_4Sb_{12}$ at 600 K.

As previous results, the Tl and In double-filled one showed *ZT* as high as 1.2. And, triple-filling was considered as an effective way to further reduce the thermal conductivity. Thus, we focused on the further effective phonon scattering by group 13 elements triple-filling and naturally formed nano-inclusions by over adding

of In. From such a motivation, the sample compositions were determined as $In_xGa_{0.02}Tl_{0.20}Co_4Sb_{12}$ (x = 0 ~ 0.30), which the filling fraction limit of In, Ga, and Tl in $CoSb_3$ based skutterudites were determined as 8%, 2% and 20% respectively according to our previous studies. Just like we had envisioned, finely dispersed nano inclusions with sizes of 20 ~ 200 nm were observed by FE-SEM. And we found an interesting phenomenon, that Tl contents in the matrix decreased with increasing the amounts of In by EDX analysis. And based on the similar carrier concentration and total filling amounts in all the samples, we determined that the valence value of In in $CoSb_3$ based skutterudites is +1 not +3. Due to, all of the samples possessed relatively high Tl contents and finely dispersed nano-inclusions on the grain boundaries, the relatively low lattice thermal conductivity was obtained. And the *ZT* of 0.72 was approached for $In_{0.30}Ga_{0.20}Tl_{0.20}Co_4Sb_{12}$ at 773 K.

Tl and K are much different in rattling frequencies. Therefore, the more broad phonons can be scattered by Tl and K co-filling, resulted in a significant reduction of lattice thermal conductivity. According to the previous reports, the filling fraction of Tl and K are 20% and 45% respectively. Moreover, when two or more foreign atoms fill into the cages simultaneously, the total filling amounts of fillers will approach to the same with the atoms has the maximum filling fraction among the filler atoms. In other words, Tl's filling fraction will be driven up when co-filling with K in which has filling fraction limits as high as 0.45. As a results, the lattice thermal conductivity as low as 0.9 $Wm^{-1}K^{-1}$ at 700 K was obtained for $Tl_{0.3}K_{0.3}Co_4Sb_{12}$. In addition, due to the high carrier concentration, the bipolar effect was successfully depressed, and the power factor also approached as high as $4.0x10^{-3}Wm^{-1}K^{-2}$, resulted in the *ZT* approached to unity at high temperature for $Tl_{0.3}K_{0.3}Co_4Sb_{12}$.

Half-Heusler compound have received much attention in recent years due to the large *S* and a very low κ. In the present study, noble metal contained PtYSb was prepared and the TE properties were investigated. Althogh, the electrical conductiviy was higher than previous data at room temperature, a considerably high power factor 2.1 x 10^{-3} $Wm^{-1}K^{-2}$ was obtained at 973 K. Although Y_2O_3 and Pt_3Y were preseted as impurity phases, the thermal conductivity showed a relatively low value,

resulted in a relative high *ZT* of 0.6 was obtained at 973 K for the bulk polycrystalline PtYSb.

Conclusions

The present work demonstrated that the group 13 elements (Ga, In, and Tl) are effective species for reduction of lattice thermal conductivity as fillers. And, the natural formation of nano-inclusions by over adding Ga or In is an positive feature as TE materials. In the present study, we also studied the TE properties of Tl and K co-filled skutterudites. This is the first try of combination by group 13 element with alkaline metal. Due to K addition, the filling amounts of Tl approached to 30%, which obviously exceeded the FFLs of Tl that was reported as 20%. And, the total filling amounts of Tl and K approached as high as 50% for $Tl_{0.3}K_{0.3}Co_4Sb_{12}$ in the nominal composition, results in a further depression of κ_{lat} than either Tl- or K- single-filling as shown in Figure C1.[1,2)]

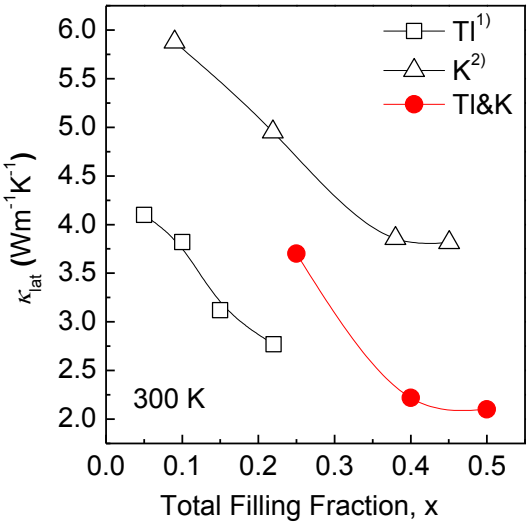

Figure C1. Comparison of lattice thermal conductivity between (Tl,K) double-filled skutterudites and the literature data.

The minimum κ_{lat} was approached as low as 0.9 $Wm^{-1}K^{-1}$ at 700 K. This study opened up a new way that no longer limited to a traditional combination of alkaline

earth and rare earth. Consider the large difference in resonant frequency in Tl-K co-filling system, such a low κ_{lat} also could be attributed to a broader phonon scattering by Tl-K co-rattling effect. In order to clarify the relationship between the difference in resonant frequency ($\Delta\omega$) and κ_{lat}, I summarized the data and plotted it as shown in Figure C1.[3,4)]

At first we expected that the larger difference in resonant frequency between two filler atoms would scatter broader range of phonons, result in a lower κ_{lat}. However, due to there are no common elements between the present work (Tl-K) and the previous literatures,[3,4)] there is no consistency in which between frequency difference and κ_{lat} was observed. In order to, clarify the effect of frequency difference on κ_{lat} in Tl-K double filled skutterudites system, the works of In-K and Ga-K double filled skutterudites systems should be studied in the future.

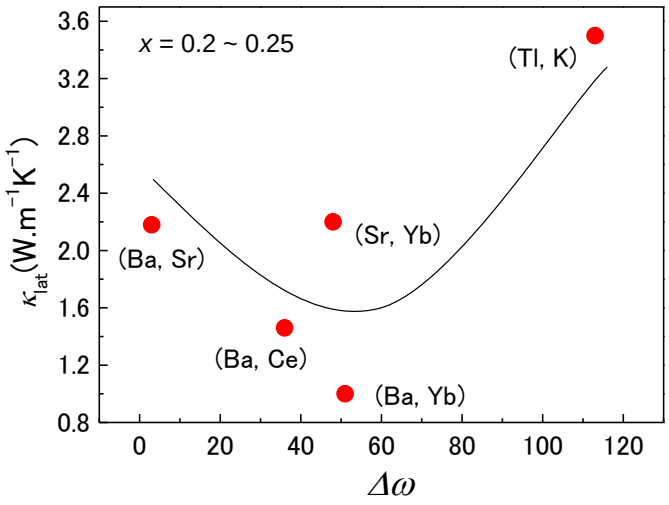

Figure C2. Relationship between the frequency difference, $\Delta\omega$ and lattice thermal conductivity, κ_{lat} of the double-filled skutterudites $(R,M)_xCo_4Sb_{12}$, which the total filling fraction in the range of x = 0.2 ~ 0.25.

In the present study, we used the most common experimental method, only for exploration the filler effects on TE properties. If the advanced experimental

methods were introduced (for example, ball milling, melt spinning, or high pressure torsion and so on.), there is still much potential to enhance the value of *ZT* for group 13 elements filled skutterudites.

Half-Heusler compounds are one of the classic bulk TE materials with a high power factor and high thermal stability. The *n*-type half-heusler compounds were well studied and the highest *ZT* approached as high as 1.5. On the contrary, the *p*-type half-heusler compounds were rarely studied and the *ZT* is much lower than *n*-type as shown in Figure C2. From module fabrication reason, the development of *p*-type half-heusler compound is necessary. PtYSb as a *p*-type half-heusler compound showed a very high *ZT* of 0.6 at 973 K. This is one of the highest value among the *p*-type half-heusler compounds up to data as shown in Figure C3. In the case of $Zr_{0.5}Hf_{0.5}CoSn_{0.8}Sb_{0.2}$, the *ZT* was increased around 50% through nano structuring technique.[5,6] Therefore, if the same technique applied to PtYSb, the *ZT* will be significantly increased further. Although, it showed a high TE performance, due to the Pt is the most precious metal, it is not possible for massive production. Therefore, Ni is the considered element use in the future work instead of Pt.

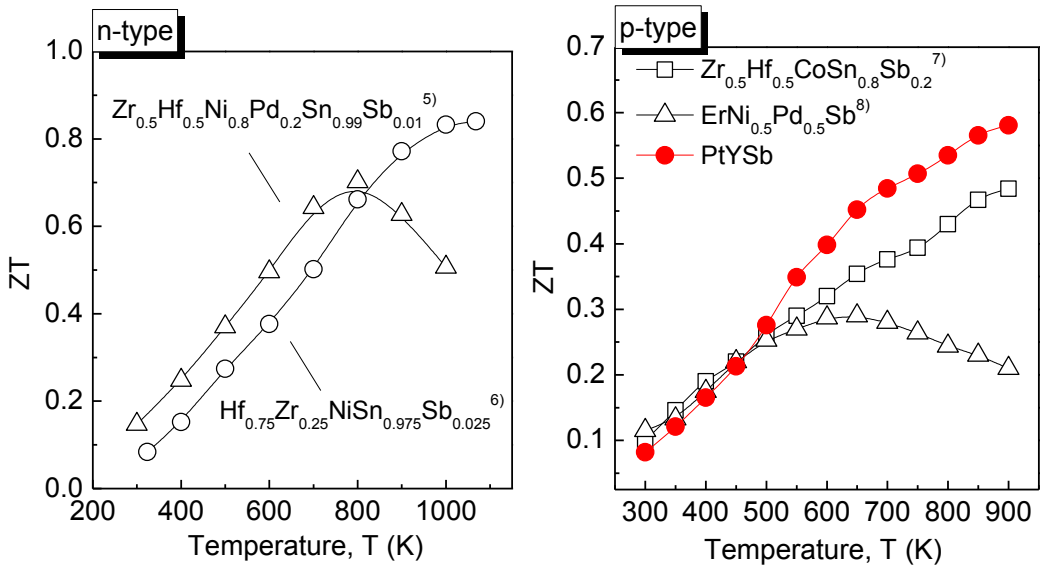

Figure C3. Comparison of *ZT* between *n*-type and *p*-type half-hausler compounds.

The electric resistivity and thermal diffusivity were measured several times for the group 13 elements filled skutterduites samples from room temperature to 773 K, and half-heusler compound from room temperature to 973 K, and the results showed good reproducibility. Thus, it can be said that the group 13 elements-filled skutterudites and PtYSb half-heusler compounds are stable in such a temperature range within our research scope. However, the durability test in a long time is necessary for practical use.

Reference

1) A. Harnwunggmoung, K. Kurosaki, T. Plirdpring, T. Sugahara, Y. Ohishi, H. Muta and S. Yamanaka, J. Appl. Phys. **110**, 013521 (2011).
2) Y.Z. Pei, L.D. Chen, W. Zhang, X. Shi, S.Q. Bai, X.Y. Zhao, Z.G. Mei, and X.Y. Li, Appl. Phys. Lett. **89**, 221107 (2006).
3) J. Yang, W. Zhang, S.Q. Bai, Z. Mei, and L.D. Chen, Appl. Phys. Lett. **90**, 192111 (2007).
4) X. Shi, H. Kong, C.P. Li, C. Uher, J. Yang, J.R. Salvador, H. Wang, L. Chen, and W. Zhang, Appl. Phys. Lett. **92**, 182101 (2008).
5) Q. Shen, L. Chen, T. Goto, T. Hirai, J. Yang, G.P. Meisner, and C. Uher, Appl. Phys. Lett. **79**, 4165 (2001).
6) G.S. Nolas, J. Poon, and M. Kanatzidis, MRS Bulletin, **31**, 199 (2006).
7) X. Yan, G. Joshi, W. Liu, Y. Lan, H. Wang, S. Lee, J.W. Simonson, S.J. Poon, T.M. Tritt, G. Chen, and Z.F. Ren, Nano Lett. 11, 556 (2011).
8) K. Kawano, K. Kurosaki, H. Muta, and S. Yamanaka, J. Appl. Phys. **104**, 013714 (2008).

Research Achievements

Publications of Articles

1. **Thermoelectric Properties of Indium-Added Skutterudites $In_xCo_4Sb_{12}$**
   Journal of Electronic Materials, **42**, 7 (2013).
   Guanghe Li, Ken Kurosaki, Yuji Ohishi, Hiroaki Muta, and Shinsuke Yamanaka
2. **High Temperature Thermoelectric Properties of Half-Heusler Compound PtYSb**
   Japanese Journal of Applied Physics, **52**, 041804 (2013).
   Guanghe Li, Ken Kurosaki, Yuji Ohishi, Hiroaki Muta, and Shinsuke Yamanaka
3. **Thermoelectric Properties of Group 13 Elements-Triple Filled Skutterudites: $In_xGa_{0.02}Tl_{0.20}Co_4Sb_{12}$**
   Materials Transactions, **Accepted** (2014.05.30).
   Guanghe Li, Ken Kurosaki, Yuji Ohishi, Hiroaki Muta, and Shinsuke Yamanaka

International Conference

1. **Thermoelectric Properties of In-added $CoSb_3$ Based Skutterudites**
   The 31st international & 10th European Conference on Thermoelectrics, Aalborg, Denmark. July 9th-12th (2012).
   Guanghe Li, Ken Kurosaki, Yuji Ohishi, Hiroaki Muta, and Shinsuke Yamanaka
2. **Effect of In-filling on Thermoelectric Properties of $CoSb_3$**
   IUMRS-International Conference on Electronic Materials, Yokohama, Japan, September 23-28 (2012).
   Guanghe Li, Ken Kurosaki, Yuji Ohishi, Hiroaki Muta, and Shinsuke Yamanaka
3. **Thermoelectric Properties of Indium-Filled Skutterudites: $In_xCo_4Sb_{12}$**
   Powder Metallurgy World Congress & Exhibition, Yokohama, Japan, October 14-18 (2012).
   Guanghe Li, Ken Kurosaki, Yuji Ohishi, Hiroaki Muta, and Shinsuke Yamanaka

4. **Effect of Group 13 Elements-Triple Filling on Thermoelectric Properties of $CoSb_3$**

   The 15th Asian Chemical Congress, Singapore, August 20-23 (2013).

   Guanghe Li, Ken Kurosaki, Yuji Ohishi, Hiroaki Muta, and Shinsuke Yamanaka

5. **Thermoelectric Properties of Group 13 Elements-Triple Filled Skutterudites: $In_xGa_{0.02}Tl_{0.20}Co_4Sb_{12}$**

   International Conference on Thermoelectrics, Kobe, Japan, June 30-July 4 (2013).

   Guanghe Li, Ken Kurosaki, Yuji Ohishi, Hiroaki Muta, and Shinsuke Yamanaka

6. **Thermoelectric Properties of Group 13 Elements Filled Skutterudites**

   Energy Materials Nanotechnology, Beijing, China, May 12-15 (2014).

   Guanghe Li, Ken Kurosaki, Yuji Ohishi, Hiroaki Muta, and Shinsuke Yamanaka

Domestic Conference

7. インジウムを添加したスクッテルダイト化合物$In_xCo_4Sb_{12}$の熱電特性

   第九回日本熱電学会学術講演会(TSJ2012), 2012年8月27-28日, 東京工業大学東工大蔵前会館.

   Guanghe Li, 黒崎　健, 大石　佑治, 牟田　浩明, 山中　伸介

8. **第13族元素を添加したスクッテルダイト化合物$In_xGa_{0.02}Tl_{0.20}Co_4Sb_{12}$($0 \leq x \leq 0.30$)の熱電特性**

   第十回日本熱電学会学術講演会(TSJ2013), 2013年9月8-9日, 名古屋大学豊田講堂.

   Guanghe Li, 黒崎　健, 大石　佑治, 牟田　浩明, 山中　伸介

ACKNOWLEDGEMENTS

I would like to acknowledge a number of people who were instrumental in the completion of this dissertation.

I would like to express my sincere gratitude to my PhD supervisor, Dr. Shisuke Yamanaka, for his scientific advice and kind guidance on my study. I am grateful to Dr. Kurosaki Ken for providing me instructive supports, patient guidance, insightful discussions and suggestions on my research during the three and a half years. He is my primary resource for getting my science questions answered and was instrumental in helping me crank out this thesis. I also have to thank the members of my PhD committee, Dr. Takao Yamamoto and Dr. Hiroshi Nishikawa for their helpful suggestions on my thesis.

I also would like to thank to Dr. Muta Hiroaki, Dr. Yuji Ohishi, Dr. Yoshinobu Miyazaki, and Dr. Yusufu Aikebaier for their enthusiastic help on my research. I thank Ms. Kazuko Terasoma sincerely, for her kind help of dealing with all kinds of things both from laboratory and school. I am also grateful to all the present and past members who I had known each other in Yamanaka Laboratory.

And I would like to thank Mr. Seongho Choi and my friends for providing support and friendship that I needed. My time at Osaka University was made enjoyable in large part due to many friends that became a part of my life. While everyone's life is really hard in Japan, but with the help of each other, our life always had a lot of fun.

Lastly, I especially thank my mom, dad, and sister. My hard-working parents have sacrificed their lives for my sister and myself and provided unconditional love and encouragement. I love them so much, and I would not have made it this far without them. They are always my motivation to overcome the difficulties ahead.

July, 2013

Guanghe Li